Title
Magnetic susceptibility anisotropy outside the central nervous system

Permalink
https://escholarship.org/uc/item/2tx609cb

Journal
NMR in Biomedicine, 30(4)

ISSN
0952-3480

Authors
Dibb, Russell
Xie, Luke
Wei, Hongjiang
et al.

Publication Date
2017-04-01

DOI
10.1002/nbm.3544

Peer reviewed

Published in final edited form as:
NMR Biomed. 2017 April ; 30(4): . doi:10.1002/nbm.3544.

Magnetic susceptibility anisotropy outside the central nervous system

Russell Dibb[1], **Luke Xie**[1,2], **Hongjiang Wei**[3], and **Chunlei Liu**[1,3]

[1]Center for In Vivo Microscopy, Department of Radiology, Duke University Medical Center, Durham, North Carolina 27710

[2]Utah Center for Advanced Imaging Research, Department of Radiology, University of Utah, Salt Lake City, Utah 84108

[3]Brain Imaging and Analysis Center, Duke University Medical Center, Durham, North Carolina, 27710

Abstract

Magnetic susceptibility-based MRI has made important contributions to the characterization of tissue microstructure, chemical composition, and organ function. This has motivated a number of studies to explore the link between microstructure and susceptibility in organs and tissues throughout the body, including the kidney, heart, and connective tissue. These organs and tissues have anisotropic magnetic susceptibility properties and cellular organizations that are distinct from the lipid organization of myelin in the brain. For instance, anisotropy is traced to the epithelial lipid orientation in the kidney, the myofilament proteins in the heart, and the collagen fibrils in the knee cartilage. The magnetic susceptibility properties of these and other tissues are quantified using specific MRI tools: susceptibility tensor imaging (STI), quantitative susceptibility mapping (QSM), and individual QSM measurements with respect to tubular and filament directions determined from diffusion tensor imaging (DTI). These techniques provide complementary and supplementary information to that produced by traditional MRI methods. In the kidney, STI can track tubules in all layers including the cortex, outer medulla, and inner medulla. In the heart, STI detected myofibers throughout the myocardium. QSM in the knee revealed three unique layers in articular cartilage by exploiting the anisotropic susceptibility features of collagen. While QSM and STI are promising tools to study tissue susceptibility, certain technical challenges must be overcome in order to realize routine clinical use. This paper reviews essential experimental findings of susceptibility anisotropy in the body, the underlying mechanisms, and the associated MRI methodologies.

Graphical abstract

Magnetic susceptibility anisotropy is observed in tissues throughout the body and spawns from a variety of organized molecular sources including the epithelial lipids in the kidney, myofilament proteins in the heart, and collagen fibrils in connective tissue. Two MRI tools, susceptibility tensor imaging and quantitative susceptibility mapping, have exploited this anisotropy to assess the

---

Correspondence: Chunlei Liu, Brain Imaging and Analysis Center, Duke University School of Medicine, 2424 Erwin Road, Suite 501, Campus Box 2737, Durham, NC 27705, USA, Fax: +1 919 681 7033, chunlei.liu@duke.edu.

microstructure and orientation of renal tubules, myofibers, and articular cartilage. Measuring susceptibility anisotropy using MRI is a promising technique for studying healthy and diseased organ tissues.

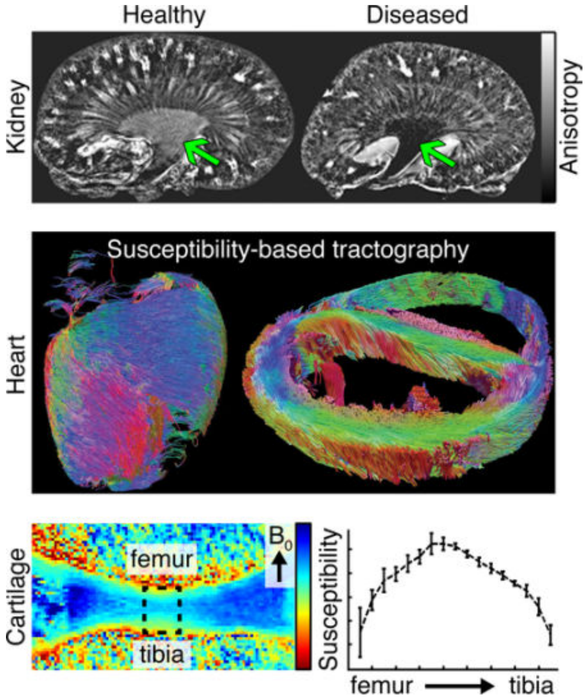

Keywords

Anisotropic magnetic susceptibility; Quantitative susceptibility mapping; Susceptibility tensor imaging; Resonance frequency shift

INTRODUCTION

Over the past few years, major advances have been made to characterize tissue microstructure, chemical composition, and organ function using magnetic susceptibility MRI (1–14). Using this technology, recent studies have shown a link between the orientation of neuronal axons in white matter and the apparent magnetic susceptibility values with respect to the B_0 field orientation (5,15,16). These findings have motivated a collection of studies to explore fibrous and tubular tissue in the body beyond the central nervous system. In particular, studies have examined the orientation-dependent magnetic susceptibility of nephron tubules in the kidney, myofibers in the heart, and collagen fibrils in connective tissue (17–22).

Local magnetic susceptibility properties of tissue have been calculated using a method called quantitative susceptibility mapping (QSM), assuming susceptibility is a scalar quantity. However, in structured tissues, anisotropic magnetic susceptibility at the molecular level ($\Delta\chi_{ML}$) can give rise to macroscopic susceptibility anisotropy ($\Delta\chi$), which indicates that magnetic susceptibility is a tensor quantity rather than a scalar quantity in those tissues.

Susceptibility anisotropy has been quantified at the molecular level with nuclear magnetic resonance and electron paramagnetic resonance spectroscopy (23–25). At the tissue level, susceptibility anisotropy has been characterized using a method called susceptibility tensor imaging (STI) (12,26,27).

In this review, we discuss the biological underpinnings of magnetic susceptibility anisotropy of organs and tissues in the body. We then review the MRI-based methods used to estimate properties of susceptibility anisotropy. Finally, we discuss the preclinical and clinical research implications, challenges, and opportunities associated with susceptibility anisotropy in the kidney, heart, and knee joint.

SOURCES OF MAGNETIC SUSCEPTIBILITY ANISOTROPY

Magnetic susceptibility anisotropy originates from a variety of molecular sources. Most biomolecules have diamagnetic (i.e. negative) susceptibility that is also anisotropic due to the non-spherical distribution of electrons. If these molecules are spatially arranged in an ordered fashion within a tissue, then they collectively will exhibit a bulk anisotropic susceptibility. A well-known example is the organized phospholipids in myelin that surround axons in the white matter of the central nervous system (12,27). In addition to lipid chains, other macromolecules and cellular contents (extracellular matrix, nucleic acids, and proteins) influence magnetic susceptibility anisotropy (12,28–32) and are found throughout the body. Here, we present the microstructural arrangement of tissue components that contributes to the MRI-observable macroscopic susceptibility anisotropy in the renal tubule, myofiber, and connective tissues such as ligament, tendon, and cartilage.

Renal tubule

The kidney is a highly structured system with organized units at the tubular and cellular level. Being the most basic functional unit, the nephron tubule is essential for solute filtration, reabsorption, secretion, and excretion. The number of nephrons is enormous, being ~1,000,000 in the human, ~30,000 in the rat, and ~20,000 in the mouse (33–35). Nephrons consist of tubules, loops, and collecting ducts that point radially from the cortex to the inner medulla. The microstructure, the lengths of nephron segments, and the distribution of long- and short-loop nephrons can substantially influence structural organization and renal function (36,37). The cellular ultrastructure of the nephron is also highly organized (Fig. 1). The renal epithelium consists of a single layer of cells that rest on a basement membrane, which serves as an anchor between the tubules and peritubular capillaries (38). One unique feature of most renal epithelial cells is the large surface area—this is critical for fluid absorption and for increasing the number of membrane proteins in the kidney as well as other organs (39–42). The surface amplification is achieved through densely arranged microvilli of the brush border on the luminal (apical) plasma membrane and basement infoldings on the basolateral membrane (Fig. 1A–C). These structures significantly increase the percentage of lipids (Fig. 1D) pointing along the tubule’s long axis.

The organized tubular structures, the basement membrane, and the organized lipids in renal epithelia are all potential sources of susceptibility anisotropy. In one study, magnetic susceptibility was measured relative to the orientation of nephron tubules by rotating the kidney with respect to the magnetic field, B_0 (21). Here, susceptibility was found to be most diamagnetic when tubules were parallel with the magnetic field, and most paramagnetic (i.e. positive) when tubules were perpendicular to the field ($\chi_{\parallel} < \chi_{\perp}$). This trend suggests that there is a diamagnetic content pointing in the direction of the long axis of the tubule. The epithelial lipids, which at the molecular level are more diamagnetic in the direction parallel to the lipid chain than in the perpendicular direction ($\chi_{ML,\parallel} < \chi_{ML,\perp}$), predominantly point along the tubule axis (Fig. 1A).

Myofiber

Known as the “engine of life,” the heart is a complex muscular organ. Cardiac muscle is distinctive in that it combines the involuntary movement features of smooth muscle with many of the organized structural features of skeletal muscle. Myocardium, the layer of muscle in between the endocardium and the epicardium, is made up of striated muscle cells, or fibers, each comprising multiple myofibrils. Within each myofibril is a serially repeating structure known as the sarcomere (Fig 2A), which acts as the fundamental structural and functional unit for muscle contraction. The structure of the sarcomere is highly organized, characterized by a lattice of thick and thin myofilaments (Fig. 2B–C). The orientation of each individual filament is roughly parallel to the long axis of the myofiber (Fig. 2D). Myofilaments are primarily constructed of myosin, tropomyosin, and actin—three proteins that are replete with polypeptide chains in the α-helix form (Fig 2E).

The peptide groups that form α-helix structures are a source of diamagnetic anisotropy in muscle tissues (32,43,44). Consequently, these peptide groups may be a source of the bulk susceptibility anisotropy measured in myocardium using MRI (17). Peptide bonds in the α-helix all lie in a plane parallel to the helix axis (Figure 2E). At the molecular level, each individual peptide group has an out-of-plane susceptibility that is more diamagnetic than its in-plane susceptibility ($\chi_{ML,\perp} < \chi_{ML,\parallel}$). This gives the peptide group a theoretical molar susceptibility anisotropy value ($\Delta\chi_{ML} = \chi_{ML,\parallel} - \chi_{ML,\perp}$) of 6.74×10^{-11} m^3/mol (SI units) or 5.36×10^{-6} cm^3/mol (CGS units) (45). Dibb et al. simulated the secondary and tertiary structures of the α-helix in sarcomeric myosin and tropomyosin (Fig. 2C–D) and showed that the aggregate effect of the magnetic asymmetry of peptide groups ($\Delta\chi_{ML}$) produces bulk susceptibility anisotropy ($\Delta\chi$) in myofibers similar to that observed with MRI (17). Cumulatively, the structure and organization of α-helix proteins also explain that myofibers perpendicular to the field appear diamagnetic ($\chi_{\perp} < 0$) and myofibers parallel to the field appear paramagnetic ($\chi_{\parallel} > 0$) relative to the reference susceptibility (17).

In addition to the peptide bonds in myosin and tropomyosin α-helices, other potential sources of anisotropy include actin, collagen, myoglobin, and lipids. Both globular and filamentous forms of actin contain α-helix structures, although they are much less uniformly organized (46) and only weakly align to an applied magnetic field (44). Collagen exhibits susceptibility anisotropy that is both directionally opposite and about half as strong as that of myofilament α-helices (32). Because it constitutes only a small fraction of myocardium relative to myofibrillar proteins (47,48), collagen’s influence on susceptibility anisotropy is likely minor in the healthy heart. In ischemic myocardium, however, elevated collagen content (49) may have greater influence over the observed bulk susceptibility anisotropy.

Deoxymyoglobin is a paramagnetic globular protein with a large molar susceptibility anisotropy of $-1.22 \pm 0.05 \times 10^{-8}$ m^3/mol (SI units) or $-9.73 \pm 0.38 \times 10^{-4}$ cm^3/mol (CGS units) (50). In heart tissue, myoglobin molecules are mobile and diffuse (51), so they are more likely to produce a bulk magnetic susceptibility shift instead of bulk susceptibility anisotropy in myocardium. Lastly, the lipids that form the sarcoplasmic reticulum surrounding individual myofibrils may be a source of susceptibility anisotropy, similar to the brain and kidney. In rodents, however, the lipid volume fraction is only ~0.03 in myocardium cells (52), whereas it is ~0.16 in brain white matter (53) and ~0.08 in the kidney (54). On the other hand, the cell volume fraction of myofibrillar mass is ~0.45–0.47 in rodent myocardium (52,55); thus, myofibrillar peptide groups still appear to be the dominant contributor to the myocardial susceptibility anisotropy visualized with MRI (17).

Connective tissue

Connective tissues are highly structured to support different tissues in the body. Their layered organization allows organs and joints to resist stretching, shearing, and compression. A vast portion of connective tissue is characterized by the abundance of the fibrous, structural protein known as collagen. Collagen fibrils (Fig. 3A–B) are composed of many molecules (Fig. 3C), each of which comprises a right-handed bundle of three parallel, left-handed polyproline II-type helices (Fig. 3D) (56–58). Unlike the right-handed α-helix proteins found in myofilament proteins, which have peptide group planes running parallel to the helix axis, the collagen triple helix contains peptide group planes oriented at approximately 45° to the fibril axis (Fig. 3E) (32). Because the most diamagnetic susceptibility is oriented normal to the peptide group plane, the net susceptibility of collagen fibrils is most diamagnetic in the direction parallel to the fibril axis ($\chi_\parallel < \chi_\perp$) (32,59). This trend is the opposite of the susceptibility anisotropy observed in skeletal and cardiac muscle fibers.

METHODS FOR MEASURING SUSCEPTIBILITY ANISOTROPY USING MRI

Measuring magnetic susceptibility anisotropy with imaging has only been conducted in a limited number of approaches. These include correlating quantitative susceptibility values with diffusion-tensor based fiber angle data, susceptibility tensor imaging (STI), and DTI-aided calculation of a cylindrically symmetric susceptibility tensor.

Correlating quantitative susceptibility with diffusion-tensor-based fiber angle

Susceptibility anisotropy can be quantified by plotting the apparent magnetic susceptibility as a function of tissue orientation. Tissue orientation is typically computed as the angle between the major eigenvector of the diffusion tensor of the tissue and the B_0 direction, assuming that DTI correctly identifies the tissue orientation; apparent magnetic susceptibility, on the other hand, is measured by quantitative susceptibility mapping (QSM) at either one or multiple object orientations. Specifically, a linear regression is performed on apparent magnetic susceptibility data as a function of the squared sine of the fiber angle with respect to the applied magnetic field. This regression can be performed for all voxels within the tissue together (especially when only one object orientation is available) or on a voxel-by-voxel basis (when multiple object orientations are available). The bulk magnetic susceptibility anisotropy can then be defined by the fitted correlation as $\Delta\chi = \chi(0°) - \chi(90°)$. This method has been used to identify magnetically anisotropic tissues in central nervous system white matter (27) and the renal tubule (Fig. 4) (21). Similar assessments of both single- and multiple-orientation QSM have confirmed the presence of susceptibility anisotropy in myocardium (Fig. 5) (17). Although single-orientation measurements require less scan time than multiple-orientation measurements, they assume homogeneous susceptibility anisotropy throughout the tissue. Susceptibility anisotropy assessments based on this method are affected by QSM quality, and thus can be limited by reconstruction artifacts that vary according to the orientation of the specimen (12,60,61). The need to acquire diffusion tensor data in addition to gradient-recalled echo (GRE) data also adds additional scan time.

Susceptibility tensor imaging

While susceptibility anisotropy can be suggested by correlating susceptibility measurements and tissue orientation, anisotropic magnetic susceptibility is better characterized using a second-order tensor. STI calculates this tensor from frequency image data acquired at a theoretical minimum of six object orientations (26). Magnetic susceptibility anisotropy can then be defined in terms of the susceptibility tensor eigenvalues as $\Delta\chi = \chi_1 - (\chi_2 + \chi_3) / 2$. Here we define χ_1, χ_2, and χ_3 as the primary (most positive), secondary, and tertiary (least positive) eigenvalues (Fig. 6). In STI, susceptibility tensor values are relative to a reference, so producing a *normalized* definition of susceptibility anisotropy is challenging even though the susceptibility anisotropy defined above ($\Delta\chi$) is independent of reference. Hence, for the purposes of STI tractography, Liu et al. defined a susceptibility index, SI = $(|\chi_1 - \chi_3| + \gamma) / \overline{\chi}$, where $|\chi_1 - \chi_3|$ is a direct measure of susceptibility anisotropy, γ s a tunable parameter to balance between susceptibility anisotropy and image contrast, and $\overline{\chi}$ is the mean susceptibility (62). Xie et al. used this definition for STI tractography of the kidney (21), but with $\gamma = 0$ so that SI could not be arbitrarily adjusted. This also facilitated comparisons between healthy and diseased kidney specimens (20). Both $\Delta\chi$ and SI do not rely on DTI data for tissue orientation information. This is particularly useful for tissues with complex chemical and structural features that may exhibit susceptibility and diffusion tensors with non-identical eigenvectors. In comparison to measures of susceptibility anisotropy, fractional anisotropy (FA) is used to identify tissue regions with substantially anisotropic diffusion (63).

DTI-aided calculation of a cylindrically symmetric susceptibility tensor

For cylindrical structures, one may assume that the secondary (χ_2) and tertiary (χ_3) eigenvalues are the same. Bulk tissue magnetic susceptibility can then be defined in the directions parallel ($\chi_\parallel$) and perpendicular ($\chi_\perp$) to the underlying tissue structure, with $\Delta\chi = \chi_\parallel - \chi_\perp$. Assuming cylindrical symmetry in the susceptibility tensor simplifies STI reconstruction by reducing the number of unknowns in the inverse problem from six to four (64). This number is further reduced to two ($\chi_\parallel$ and $\chi_\perp$) by incorporating DTI information, specifically by assuming that the principal susceptibility eigenvectors are equal to the principal diffusion eigenvectors (64–66). Having fewer unknown quantities improves the conditioning of the STI inverse problem, and a cylindrically symmetric susceptibility tensor can be defined, in practice, with as few as three GRE image orientations (66). Nevertheless, these assumptions may not apply to most organ tissues. In the event that they do apply, diffusion tensor data are still required to estimate susceptibility anisotropy. Susceptibility anisotropy measurement techniques that are able to incorporate other types of information—such as diffusion (66) or relaxation (18) tensor data—will aid in the discovery and understanding of the mechanisms underlying tissue susceptibility in healthy and diseased tissue. Such developments have the potential to increase the sensitivity of MRI in applications such as diagnosing and monitoring disease.

APPLICATIONS OF MAGNETIC SUSCEPTIBILITY ANISOTROPY

Mapping renal tubule orientations with susceptibility tensor imaging

STI has been successfully demonstrated to detect tubules in mouse kidney specimens (21). Briefly, STI was achieved by acquiring phase image data using a 3D multi-echo GRE sequence at 12 object orientations with respect to the magnetic field (9.4 T). DTI was acquired using a 3D diffusion-weighted spin-echo sequence and 12 gradient directions (diffusion time of 17 ms without contrast agent and 5.7 ms with contrast agent). The b-value was maintained at 1,500 s/mm^2. An isotropic resolution of 55×55×55 mm^3 was acquired for both STI and DTI of kidneys with contrast agent. STI and DTI tractography were then performed based on the eigenvectors associated with the tertiary (most diamagnetic) susceptibility and the primary (most positive) diffusion eigenvalue, respectively.

STI was able to track more tubular segments throughout the organ compared to a traditional DTI protocol. This is because STI exhibited strong anisotropy throughout the kidney. In kidney specimens with contrast agent, SI ($\gamma = 0$) was measured at 0.36 in the inner medulla (IM), 0.29 in the outer medulla (OM), and 0.19 in the cortex (CO). Based on a different calculation of anisotropy, FA from DTI was measured at 0.27 in the IM, 0.17 in the OM, and 0.14 in the CO. STI detected tubular tracts in the IM and OM, while DTI was mostly limited to the IM (Fig. 7).

The difference between STI and DTI can be explained by the length scale and dimensions of the renal tubules throughout the kidney. The kidney has both straight and tortuous segments of the nephron tubule. Anisotropy measurements are greater and tractography succeeds mostly in the straight segments. These segments consist of the ascending thin limbs, the medullary thick ascending limbs, and the collecting ducts (inner diameters included in Table 1) (37,67). In general, DTI performed well in thin coherent structures and was governed by the average displacement of a Brownian particle:

$$\overline{x^2}=2Dt$$

where $\overline{x^2}$ is the mean squared displacement, D is the water diffusion coefficient, and t is the time of diffusion or time between diffusion gradients used for DTI. The average displacement was 5.2 μm based on the diffusion time of 5.7 ms with contrast agent. At this length scale, DTI was mostly limited to the ascending thin limbs. In the large tubules, water diffusion would appear to be isotropic and DTI was not successful in representing the anisotropic structures. In order to detect such large diameter structures, diffusion times would need to be greater than 470 ms, when the MRI signal is significantly depleted. Spin-echo DTI represents only one form of diffusion imaging, and alternative methods such as diffusion imaging using stimulated echoes (68), q-ball imaging (69), and diffusion spectrum imaging (70) might be able to detect larger structures. STI detected all straight segments regardless of the length scale.

Reduced susceptibility anisotropy in models of kidney disease

STI studies of diseased kidneys indicate that injury can occur at the microstructural level. Susceptibility anisotropy changes were measured in an angiotensin receptor knockout model (AT1a −/− AT1b −/−) and a diabetic nephropathy model (Akita) (20). Studies were limited to one kidney per model and one control. Here, susceptibility anisotropy was significantly reduced compared to diffusion anisotropy (Fig. 8). In the center of the IM, FA from DTI was reported as 0.22 in C57BL/6 (wild type), 0.21 in Akita, and 0.17 in AT1a −/− AT1b −/−. In contrast, SI from STI ($\gamma = 0$) was reported as 0.29 in C57BL/6 (wild type), 0.03 in Akita, and 0.04 in AT1a −/− AT1b −/−. This is equivalent to a SI reduction of 86–90% in diseased kidneys compared to normal. On the other hand, FA was reduced by only 5–23%. Similarly, tractography with STI was reduced relative to DTI (Fig. 9). Compared to the normal kidney, DTI revealed fewer tracts in the IM of diseased kidneys. STI virtually did not track any tubules in the same area. The similar diffusion anisotropy in the normal and diseased kidneys suggests that the renal tubules were mostly intact. Conversely, the large susceptibility anisotropy changes suggest injury to the microstructure inside the epithelium. With more sensitive susceptibility anisotropy measurement tools (see *Technical Considerations*), it may be possible to detect microstructural damages in patients with angiotensin receptor deficiency and diabetic nephropathy.

The origin of susceptibility anisotropy has been hypothesized to be the organized lipids on the microvillis, basolateral infoldings, and mitochondria (21). This hypothesis can be supported in part by disruption of the aligned lipids leading to reduced anisotropy and limited tubular tracking. Ischemia reperfusion of the kidney is an injury that leads to tubular obstruction and damage, inhibition of cellular metabolism of mitochondria, mitochondrial swelling, brush border swelling, membrane destruction, and loss of cell polarity (71–76). This model of cellular disorganization may also explain some of the results in the angiotensin receptor knockout and diabetic nephropathy models. Future work in this area will be critical to the understanding of susceptibility anisotropy in the renal system.

Susceptibility-based myocardial fiber mapping

Myocardial fiber organization and structure are integral elements of myocardial stress and strain (77) and are altered by cardiac hypertrophy (78) and infarction (79,80). Using MRI to verify the susceptibility anisotropy of myocardium and its underlying mechanisms may lead to more sensitive and/or complementary techniques for examining the myofiber content and structure of healthy and diseased hearts. Though DTI is typically used for myocardial fiber mapping (80–84), susceptibility contrast MRI has demonstrated additional sensitivity to chemical and structural tissue properties, such as the presence of lipids in bilayer membranes and renal epithelia (5,21).

Susceptibility-tensor-based tractography of a whole heart specimen was demonstrated by Dibb et al. (18). Briefly, STI data were reconstructed from phase data acquired at 9.4 T using a GRE sequence with 8 echoes (array = 512 × 512 × 512, isotropic resolution = 30 μm, TR = 50 ms, flip angle = 50°, $TE_1/\Delta TE/TE_8$ = 3.0/5.5/41.5 ms) with the Gd-enhanced myocardium specimen positioned in 18 different orientations with respect to the magnetic field. DTI data were acquired with a 3D diffusion-weighted spin-echo sequence (array = 400 × 300 × 300, isotropic resolution = 30 μm, TR = 50 ms, TE=15.4 ms): one scan with b = 0 s/mm^2, 12 diffusion-encoded scans with b = 1,000 s/mm^2 and diffusion time = 9.6 ms. Susceptibility tractography was then performed based on the eigenvector associated with the primary (most paramagnetic) susceptibility eigenvalue. The study showed that STI could resemble DTI fiber mapping and tractography in normal mouse hearts (Fig. 10). Susceptibility-based myofiber tractography breaks down in thin-walled regions of the heart, such as the right ventricle wall. STI fiber mapping also suffers from artifacts spawning from incorrect or incomplete phase data, although these errors are mitigated by incorporating orientation-dependent R_2* relaxation information (18). Despite these improvements, the study still showed substantial differences between STI and DTI. Tractography differences may be indicative of the different structural and chemical mechanisms underlying anisotropic susceptibility and diffusion tensors. In the diffusion tensor, for instance, the primary eigenvector indicates the myofiber orientation, whereas the fiber sheet structure of the heart dictates that the secondary and tertiary eigenvectors consistently point in the transmural direction and in a direction parallel to the epicardial tangent plane, respectively (83). The fiber sheet structure may have a much different influence over the primary, secondary, and tertiary susceptibility eigenvectors. Furthermore, the influence of myofilament proteins, collagen, and lipids may play a more prominent role in determining the tissue susceptibility tensor due to the chemical sensitivity of susceptibility imaging.

The susceptibility anisotropy of the myofiber has been attributed to the arrangement of magnetically anisotropic peptide bonds in myofilament proteins (17). This hypothesis may be tested in a model of cardiac hypertrophy. Though hypertrophy is characterized by a thickening of the heart wall and an increase in total heart mass, it also yields higher actin and myosin concentrations in myocardium (49). Detecting increased susceptibility anisotropy in hypertrophic myocardium would support the claim that these myofilament proteins are the source of the orientation-dependent susceptibility contrast in MRI. Measurements of susceptibility anisotropy may also be useful in assessing increases in myocardial collagen content, which is associated with ischemia (49), infarction (85), and hypertension (86).

Quantitative susceptibility mapping of the knee joint

Collagen-containing connective tissues exhibit anisotropic susceptibility (87)—Krasnosselskaia et al. demonstrated that the frequency contrast produced by bovine tendon varied according to the orientation of the specimen with respect to the magnetic field (Fig. 11) (88). Investigating and evaluating the anisotropic susceptibility properties of connective tissue structures in the knee joint could potentially aid in assessing knee joint diseases and disorders. The knee is one of the most important joints in the human body and has complex interfaces between bones, muscles, and fat and several connective tissue structures including tendons, ligaments, cartilage, and menisci. Each connective tissue has distinct functional requirements that determine the orientation and arrangement of its collagen fibrils. For example, Fig. 12 shows that collagen fibril orientations in articular cartilage vary from radial in the deeper layers to isotropic in the middle layers to tangential in the superficial layers. The radial fibrils resist compression within the joint, whereas the tangential fibers resist shear at the interface between the femoral and tibial cartilage (89). This produces particularly interesting QSM contrast, since the apparent magnetic susceptibility of connective tissue depends on the collagen fibril orientation in the external magnetic field (87).

Wei et al. found that QSM reveals the multilayer structure of articular cartilage (22). This finding is supported by R_2* mapping, which is a commonly used indicator of connective tissue integrity (90). Fig. 13A–B shows that susceptibility and R_2* yield a similar, symmetric contrast pattern in the femoral cartilage (from femur bone surface to synovial fluid) and tibial cartilage (from tibia bone surface to synovial fluid) (22). Such susceptibility variation may be due to the orientation of collagen fibrils within the cartilage (compare to Fig. 12) relative to the static magnetic field, B_0. Fig. 13D shows that layers where collagen fibers are mostly parallel to B_0, the susceptibility values are more diamagnetic, as seen in the deep zone (yellow). Where collagen fibrils are mostly oriented perpendicular to the B_0 field, the susceptibility values are more paramagnetic, as seen in the superficial tangential zone (blue). This finding is supported by a previous study, which explained that collagen has the smallest numerical diamagnetism when it is perpendicular to the applied magnetic field (32). Alternatively, the susceptibility gradients observed in the cartilage layers may be a consequence of varying of isotropic susceptibility.

The macroscopic susceptibility anisotropy ($\Delta\chi$) of collagen comes from the diamagnetic anisotropy of the peptide group at the molecular level ($\Delta\chi_{ML}$). Cumulatively, these organized peptide groups yield the greatest diamagnetism in the direction of the collagen molecule long axis (32). Though these peptide groups also underlie the bulk susceptibility anisotropy of myofibers, the directionality is opposite in collagen due to the oblique orientations of the peptide groups relative to the fibril axis (compare Fig. 3D and Fig. 4E). This is analogous to how the molecular level susceptibility anisotropy ($\Delta\chi_{ML}$) of the lipid chain generates bulk susceptibility anisotropy ($\Delta\chi = \chi_{\parallel} - \chi_{\perp}$) that is positive in axon fiber bundles and negative in the renal tubule. Hence, both the molecular susceptibility anisotropy sources and their microstructural organization are important determinants of the macroscopic susceptibility anisotropy observed with MRI. Elucidating these and other molecular and organizational sources of anisotropy is one of the many challenges currently being addressed in susceptibility anisotropy research.

CHALLENGES, LIMITATIONS, AND OPPORTUNITIES

Technical considerations

One of the major challenges of measuring susceptibility anisotropy using STI or other similar methods is the range of object orientations that must be sampled. Ideally, a large range of angles is desired to improve the conditioning of the inverse problem. In STI studies of the mouse heart and kidney (18,21), the orientations cover a hemisphere fairly equally (manually reoriented specimen positions were determined by registration). For example, the unit vectors of 12 orientations from a study of the mouse kidney *ex vivo* (21) are included in Fig. 14A. By contrast, the unit vectors of 12 orientations from a study of the brain *in vivo* (91) are included in Fig. 14B. While STI may be performed using a very limited range of angles as demonstrated in the brain, the poor conditioning of the inverse problem can result in tensor calculation errors (92). These errors would be especially prevalent in body STI, where achieving a minimum of six independent body positions would be very challenging. Realistically, body STI may only be practical if the number of orientations were reduced to three or fewer. The DTI-aided calculation of a cylindrically symmetric susceptibility tensor method described earlier in this review (66,93) reduces the number of orientations needed to solve the susceptibility tensor elements to two or three. In addition to the challenge of angle coverage *in vivo*, the acquisition time is equally important. Maintaining a certain orientation of the torso during a scan, for instance, can be uncomfortable. To compensate, tools have been developed to speed up STI acquisition time. Accelerated imaging using Wave-CAIPI permits imaging a 240 × 240 × 168 array in 90 seconds per orientation with very little noise amplification (91).

Object reorientation and image acquisition for *ex vivo* STI are facilitated by specialized hardware and a large coil-to-object volume ratio. Fig. 15 shows an apparatus designed for STI data acquisition of mouse kidney and heart specimens in a 9.4 T vertical-bore magnet (21). In between each GRE scan, the sphere containing the specimen (Fig. 15C) is manually repositioned in a new orientation relative the applied magnetic field. Preferably, this reorientation would be mechanically automated in order to ensure consistent rotation angles and minimize disruption to the experimental settings. Such a setup would require two axes of rotation in order to provide adequate orientation coverage. Automatic sample reorientation has been demonstrated with one axis of rotation for a study of orientation-dependent MRI signal in articular cartilage (90) and with three axes of rotation using a goniometer for electron spin resonance studies (94). While these approaches are important for understanding physical mechanisms, they do not directly translate to clinical usage.

In addition to hardware, tools such as contrast agent and multi-echo pulse sequences accelerate STI data acquisition. Though not necessary, contrast agent decreases the scan time needed for *ex vivo* STI by shortening the T_1 of the tissue and allowing for shorter repetition times. In a study of the mouse kidney, contrast agent reduced the acquisition time per orientation by a factor of four while even improving SNR relative to non-contrast acquisitions (21). Imaging without contrast agent, however, is desirable for clinical settings. One alternative to contrast agent that can be used in both clinical and preclinical STI is averaging multi-echo frequency map data (95). Interestingly, the SNR gains of multi-echo averaging may be greater in the absence of contrast agent (21) since Gd and similar agents shorten T_2* and effectively reduce the number of echo images with usable signal. In our experience, the benefits of multi-echo frequency map averaging coupled with the sensitivity of GRE image phase allow for quality non-contrast STI data to be acquired *ex vivo* with relatively short repetition times (~150–200 ms when acquiring 12 object orientations with ~50-μm isotropic resolution at 9.4 T).

Limitations of STI in the kidney

In the kidney, the source of susceptibility anisotropy is hypothesized to originate from epithelial microstructure and cellular lipid organization. Segments of renal tubule have varying epithelial ultrastructure, changing microvilli density, and distinct microfolds across the proximal tubules, thin limbs, distal tubules, and collecting ducts (37,96–99). All of these can affect the lipid organization and structural anisotropy. Thus, a reduction in susceptibility anisotropy in one segment of the nephron may be due to normal physiology and not necessarily due to renal injury. The susceptibility anisotropies in (20,21) were reported using the susceptibility index (SI), and were calculated using an unreferenced mean susceptibility. On the other hand, $\Delta\chi$ does not depend on a reference value. SI can be very helpful for tractography purposes (62). Nonetheless, selecting a reference susceptibility for mean values or SI will be critical for comparing healthy and diseased kidney tissues in the future. For STI to be conducted in clinical studies, careful baseline data will need to be acquired to assess kidney disease.

Limitations of measuring susceptibility anisotropy in the heart

Myocardium has two anatomical compartments with distinct signal contributions: intracellular and extracellular (100). One microstructural model study suggests that multi-pool relaxation strongly affects susceptibility contrast and anisotropy in muscle tissue (17) similar to what is seen in models of central nervous system white matter (16,101). This relaxation is potentially affected by intracellular pH changes and tissue fixation. Furthermore, one must use caution when interpreting data from Gd-enhanced STI of the myocardium, since it has been shown that contrast agent remains highly concentrated in the extracellular volume of muscle tissue, where it disproportionally shortens relaxation times relative to the intracellular volume (102). As myocardial susceptibility imaging is a relatively new field, the impact of pH changes, tissue fixation, and contrast agents on susceptibility anisotropy in the heart remains unclear.

Future directions

STI may be beneficial in a variety of other coherent and fibrous structures in the body. These include bone, skeletal muscle, and epithelia of duct systems in the liver, pancreas, breast, and gall bladder. More studies are needed to verify the molecular sources that contribute to the bulk susceptibility anisotropy observed in the body. In particular, studies of animal models and human patients with known alterations in the relevant molecular sources are critically needed.

CONCLUSION

Magnetically anisotropic tissues are prevalent throughout the body. Studies suggest that the organized molecular mechanisms of this susceptibility anisotropy include epithelial lipids in the renal tubule, myofilament proteins in the myofiber, and collagen in connective tissues. Susceptibility-based tools such as STI and QSM can assess nephron segments in the kidney where DTI fails, yield alternative methods for myocardial tissue analysis and fiber mapping, and reveal in detail the structure of connective tissues such as articular cartilage. Despite the practical challenges of these techniques, including object reorientation and prolonged scan time, quantitatively assessing susceptibility anisotropy is a promising method for studying healthy and diseased organ tissues.

Acknowledgments

The authors wish to thank the Center for In Vivo Microscopy of Duke University, particularly G. Allan Johnson, PhD, Gary Cofer, MS, and Yi Qi, MD, for their assistance in several of the imaging experiments described in this review and Sally Zimney for her help in preparing the manuscript. This work was supported in part by the National Institutes of Health through NIBIB P41 EB015897, T32 EB001040, NIMH R01 MH096979, Office of the Director 1S10ODO10683-01, and NHLBI R21 HL122759, and by the National Multiple Sclerosis Society through grant RG4723.

Glossary/abbreviations used

CO	Cortex of the kidney
DTI	Diffusion tensor imaging
FA	Fractional anisotropy
GRE	Gradient-recalled echo
IM	Inner medulla of the kidney
MRI	Magnetic resonance imaging
OM	Outer medulla of the kidney
QSM	Quantitative susceptibility mapping
SI	Susceptibility index
STI	Susceptibility tensor imaging

References

1. Shmueli K, de Zwart JA, van Gelderen P, Li T-Q, Dodd SJ, Duyn JH. Magnetic susceptibility mapping of brain tissue in vivo using MRI phase data. Magn Reson Med. 2009; 62(6):1510–1522. [PubMed: 19859937]
2. Deistung A, Schäfer A, Schweser F, Biedermann U, Turner R, Reichenbach JR. Toward in vivo histology: A comparison of quantitative susceptibility mapping (QSM) with magnitude-, phase-, and R2*-imaging at ultra-high magnetic field strength. NeuroImage. 2013; 65:299–314. [PubMed: 23036448]
3. Wharton S, Bowtell R. Effects of white matter microstructure on phase and susceptibility maps. Magn Reson Med. 2015; 73(3):1258–1269. [PubMed: 24619643]
4. Schweser F, Deistung A, Lehr BW, Reichenbach JR. Quantitative imaging of intrinsic magnetic tissue properties using MRI signal phase: an approach to in vivo brain iron metabolism? NeuroImage. 2011; 54(4):2789–2807. [PubMed: 21040794]
5. Liu C, Li W, Johnson GA, Wu B. High-field (9.4 T) MRI of brain dysmyelination by quantitative mapping of magnetic susceptibility. NeuroImage. 2011; 56(3):930–938. [PubMed: 21320606]
6. Bilgic B, Pfefferbaum A, Rohlfing T, Sullivan EV, Adalsteinsson E. MRI estimates of brain iron concentration in normal aging using quantitative susceptibility mapping. NeuroImage. 2012; 59(3): 2625–2635. [PubMed: 21925274]

7. Schafer A, Forstmann BU, Neumann J, Wharton S, Mietke A, Bowtell R, Turner R. Direct visualization of the subthalamic nucleus and its iron distribution using high-resolution susceptibility mapping. Hum Brain Mapp. 2012; 33(12):2831–2842. [PubMed: 21932259]
8. Sharma SD, Hernando D, Horng DE, Reeder SB. Quantitative susceptibility mapping in the abdomen as an imaging biomarker of hepatic iron overload. Magn Reson Med. 2015; 74(3):673–683. [PubMed: 25199788]
9. Chen Z, Liu J, Calhoun VD. Susceptibility-based functional brain mapping by 3D deconvolution of an MR-phase activation map. J Neurosci Methods. 2013; 216(1):33–42. [PubMed: 23528239]
10. Bianciardi M, van Gelderen P, Duyn JH. Investigation of BOLD fMRI resonance frequency shifts and quantitative susceptibility changes at 7 T. Hum Brain Mapp. 2014; 35(5):2191–2205. [PubMed: 23897623]
11. Balla DZ, Sanchez-Panchuelo RM, Wharton SJ, Hagberg GE, Scheffler K, Francis ST, Bowtell R. Functional quantitative susceptibility mapping (fQSM). NeuroImage. 2014; 100:112–124. [PubMed: 24945672]
12. Lee J, Shmueli K, Fukunaga M, van Gelderen P, Merkle H, Silva AC, Duyn JH. Sensitivity of MRI resonance frequency to the orientation of brain tissue microstructure. Proc Natl Acad Sci U S A. 2010; 107(11):5130–5135. [PubMed: 20202922]
13. van Gelderen P, Mandelkow H, de Zwart JA, Duyn JH. A torque balance measurement of anisotropy of the magnetic susceptibility in white matter. Magn Reson Med. 2015; 74(5):1388–1396. [PubMed: 25399830]
14. Wei H, Dibb R, Zhou Y, Sun Y, Xu J, Wang N, Liu C. Streaking artifact reduction for quantitative susceptibility mapping of sources with large dynamic range. NMR Biomed. 2015; 28(10):1294–1303. [PubMed: 26313885]
15. Lee J, Shmueli K, Kang BT, Yao B, Fukunaga M, van Gelderen P, Palumbo S, Bosetti F, Silva AC, Duyn JH. The contribution of myelin to magnetic susceptibility-weighted contrasts in high-field MRI of the brain. NeuroImage. 2012; 59(4):3967–3975. [PubMed: 22056461]
16. Wharton S, Bowtell R. Fiber orientation-dependent white matter contrast in gradient echo MRI. Proc Natl Acad Sci USA. 2012; 109(45):18559–18564. [PubMed: 23091011]
17. Dibb R, Qi Y, Liu C. Magnetic susceptibility anisotropy of myocardium imaged by cardiovascular magnetic resonance reflects the anisotropy of myocardial filament alpha-helix polypeptide bonds. J Cardiov Magn Reson. 2015; 17(1):60.
18. Dibb, R., Liu, C. Whole-heart myofiber tractography derived from conjoint relaxation and susceptibility tensor imaging. Proceedings of the 23nd Annual ISMRM; Toronto, Canada. 2015. p. 287
19. Xie L, Sparks MA, Li W, Qi Y, Liu C, Coffman TM, Johnson GA. Quantitative susceptibility mapping of kidney inflammation and fibrosis in type 1 angiotensin receptor-deficient mice. NMR Biomed. 2013; 26(12):1853–1863. [PubMed: 24154952]
20. Xie, L., Dibb, R., Gurley, SB., Liu, C., Johnson, GA. Susceptibility tensor imaging reveals reduced anisotropy in renal nephropathy. Proceedings of the 23nd Annual ISMRM; Toronto, Canada. 2015. p. 463
21. Xie L, Dibb R, Cofer GP, Li W, Nicholls PJ, Johnson GA, Liu C. Susceptibility tensor imaging of the kidney and its microstructural underpinnings. Magn Reson Med. 2015; 73(3):1270–1281. [PubMed: 24700637]
22. Wei, H., Wang, B., Zong, X., Lin, W., Wang, N., Liu, C. Imaging magnetic susceptibility of the human knee joint at 3 and 7 Tesla. Proceedings of the 23nd Annual ISMRM; Toronto, Canada. 2015. p. 288
23. Tjandra N, Bax A. Direct measurement of distances and angles in biomolecules by NMR in a dilute liquid crystalline medium. Science (New York, NY). 1997; 278(5340):1111–1114.
24. Prestegard JH. New techniques in structural NMR–anisotropic interactions. Nat Struct Biol. 1998; 5(Suppl):517–522. [PubMed: 9665182]
25. Opella SJ. NMR and membrane proteins. Nat Struct Biol. 1997; 4(Suppl):845–848. [PubMed: 9377156]
26. Liu C. Susceptibility tensor imaging. Magn Reson Med. 2010; 63(6):1471–1477. [PubMed: 20512849]

27. Li W, Wu B, Avram AV, Liu C. Magnetic susceptibility anisotropy of human brain in vivo and its molecular underpinnings. NeuroImage. 2012; 59(3):2088–2097. [PubMed: 22036681]

28. Lounila J, Ala-Korpela M, Jokisaari J, Savolainen MJ, Kesäniemi YA. Effects of orientational order and particle size on the NMR line positions of lipoproteins. Phys Rev Lett. 1994; 72(25): 4049–4052. [PubMed: 10056366]

29. Maret G, Schickfus MV, Mayer A, Dransfeld K. Orientation of Nucleic-Acids in High Magnetic-Fields. Phys Rev Lett. 1975; 35(6):397–400.

30. Scholz F, Boroske E, Helfrich W. Magnetic anisotropy of lecithin membranes. A new anisotropy susceptometer. Biophys J. 1984; 45(3):589–592. [PubMed: 6713071]

31. Torbet J. Fibrin assembly after fibrinopeptide A release in model systems and human plasma studied with magnetic birefringence. Biochem J. 1987; 244(3):633–637. [PubMed: 3446182]

32. Worcester DL. Structural origins of diamagnetic anisotropy in proteins. Proc Natl Acad Sci U S A. 1978; 75(11):5475–5477. [PubMed: 281695]

33. Baines AD, de Rouffignac C. Functional heterogeneity of nephrons. II. Filtration rates, intraluminal flow velocities and fractional water reabsorption. Pflugers Arch. 1969; 308(3):260–276. [PubMed: 5813954]

34. Fogelgren B, Yang S, Sharp IC, Huckstep OJ, Ma W, Somponpun SJ, Carlson EC, Uyehara CF, Lozanoff S. Deficiency in Six2 during prenatal development is associated with reduced nephron number, chronic renal failure, and hypertension in Br/+ adult mice. Am J Physiol Renal Physiol. 2009; 296(5):F1166–1178. [PubMed: 19193724]

35. Smith, HW. The kidney: structure and function in health and disease. New York: Oxford University Press; 1951. p. xxiip. 1049

36. Zhai XY, Thomsen JS, Birn H, Kristoffersen IB, Andreasen A, Christensen EI. Three-dimensional reconstruction of the mouse nephron. J Am Soc Nephrol. 2006; 17(1):77–88. [PubMed: 16319188]

37. Christensen, EI., Wagner, CA., Kaissling, B. Uriniferous Tubule: Structural and Functional Organization. Compr Physiol: John Wiley & Sons, Inc; 2011.

38. Kaissling B, Le Hir M. The renal cortical interstitium: morphological and functional aspects. Histochem Cell Biol. 2008; 130(2):247–262. [PubMed: 18575881]

39. Guan ZZ, Xiao KQ, Zeng XY, Long YG, Cheng YH, Jiang SF, Wang YN. Changed cellular membrane lipid composition and lipid peroxidation of kidney in rats with chronic fluorosis. Arch Toxicol. 2000; 74(10):602–608. [PubMed: 11201667]

40. Sampaio JL, Gerl MJ, Klose C, Ejsing CS, Beug H, Simons K, Shevchenko A. Membrane lipidome of an epithelial cell line. Proc Natl Acad Sci U S A. 2011; 108(5):1903–1907. [PubMed: 21245337]

41. Kawai K, Fujita M, Nakao M. Lipid components of two different regions of an intestinal epithelial cell membrane of mouse. Biochim Biophys Acta. 1974; 369(2):222–233. [PubMed: 4371841]

42. Millingt, Pf, Critchle, Dr. Lipid Composition of Brush Borders of Rat Intestinal Epithelial Cells. Life Sci Pt 1 Physi. 1968; 7(15P1):839–&.

43. Arnold W, Steele R, Mueller H. On the magnetic asymmetry of muscle fibers. Proc Natl Acad Sci USA. 1958; 44(1):1–4. [PubMed: 16590140]

44. Torbet J, Dickens MJ. Orientation of skeletal muscle actin in strong magnetic fields. FEBS letters. 1984; 173(2):403–406. [PubMed: 6745445]

45. Pauling L. Diamagnetic anisotropy of the peptide group. Proc Natl Acad Sci USA. 1979; 76(5): 2293–2294. [PubMed: 287071]

46. Kabsch W, Mannherz HG, Suck D, Pai EF, Holmes KC. Atomic structure of the actin: DNase I complex. Nature. 1990; 347(6288):37–44. [PubMed: 2395459]

47. Bradshaw AD, Baicu CF, Rentz TJ, Van Laer AO, Bonnema DD, Zile MR. Age-dependent alterations in fibrillar collagen content and myocardial diastolic function: role of SPARC in post-synthetic procollagen processing. Am J Physiol Heart Circ Physiol. 2010; 298(2):H614–622. [PubMed: 20008277]

48. Hunter RJ, Patel VB, Miell JP, Wong HJ, Marway JS, Richardson PJ, Preedy VR. Diarrhea reduces the rates of cardiac protein synthesis in myofibrillar protein fractions in rats in vivo. J Nutr. 2001; 131(5):1513–1519. [PubMed: 11340109]

49. Frederiksen DW, Hoffnung JM, Frederiksen RT, Williams RB. The structural proteins of normal and diseased human myocardium. Circ Res. 1978; 42(4):459–466. [PubMed: 147144]

50. Bertini I, Luchinat C, Turano P, Battaini G, Casella L. The Magnetic Properties of Myoglobin as Studied by NMR Spectroscopy. Chem Eur J. 2003; 9(10):2316–2322. [PubMed: 12772306]

51. Gros G, Wittenberg BA, Jue T. Myoglobin's old and new clothes: from molecular structure to function in living cells. J Exp Biol. 2010; 213(16):2713–2725. [PubMed: 20675540]

52. Sachs HG, Colgan JA, Lazarus ML. Ultrastructure of the aging myocardium: A morphometric approach. Am J Anat. 1977; 150(1):63–71. [PubMed: 930852]

53. Naito A, Nagao T, Obata M, Shindo Y, Okamoto M, Yokoyama S, Tuzi S, Saito H. Dynorphin induced magnetic ordering in lipid bilayers as studied by (31)P NMR spectroscopy. Biochim Biophys Acta. 2002; 1558(1):34–44. [PubMed: 11750262]

54. Lindheimer MD, Katz AI, Koeppen BM, Ordóñez NG, Oparil S. Kidney function and sodium handling in the pregnant spontaneously hypertensive rat. Hypertension. 1983; 5(4):498–506. [PubMed: 6862576]

55. Wittenberg JB, Wittenberg BA. Myoglobin function reassessed. J Exp Biol. 2003; 206(12):2011–2020. [PubMed: 12756283]

56. Shoulders MD, Raines RT. Collagen structure and stability. Annu Rev Biochem. 2009; 78:929–958. [PubMed: 19344236]

57. Rich A, Crick FH. The structure of collagen. Nature. 1955; 176(4489):915–916. [PubMed: 13272717]

58. Cowan PM, McGavin S, North AC. The polypeptide chain configuration of collagen. Nature. 1955; 176(4492):1062–1064. [PubMed: 13272747]

59. Torbet J, Ronziere MC. Magnetic alignment of collagen during self-assembly. Biochem J. 1984; 219(3):1057–1059. [PubMed: 6743242]

60. He X, Yablonskiy DA. Biophysical mechanisms of phase contrast in gradient echo MRI. Proc Natl Acad Sci USA. 2009; 106(32):13558–13563. [PubMed: 19628691]

61. Li J, Chang S, Liu T, Wang Q, Cui D, Chen X, Jin M, Wang B, Pei M, Wisnieff C, Spincemaille P, Zhang M, Wang Y. Reducing the object orientation dependence of susceptibility effects in gradient echo MRI through quantitative susceptibility mapping. Magn Reson Med. 2012; 68(5):1563–1569. [PubMed: 22851199]

62. Liu C, Li W, Wu B, Jiang Y, Johnson GA. 3D fiber tractography with susceptibility tensor imaging. NeuroImage. 2012; 59(2):1290–1298. [PubMed: 21867759]

63. Basser PJ, Pierpaoli C. Microstructural and physiological features of tissues elucidated by quantitative-diffusion-tensor MRI. Journal of magnetic resonance Series B. 1996; 111(3):209–219. [PubMed: 8661285]

64. Li X, Vikram DS, Lim IAL, Jones CK, Farrell JAD, van Zijl PCM. Mapping magnetic susceptibility anisotropies of white matter in vivo in the human brain at 7 T. NeuroImage. 2012; 62(1):314–330. [PubMed: 22561358]

65. Wharton, SJ., Bowtell, R. A simplified approach for anisotropic susceptibility map calculation. Proceedings of the 19th Annual ISMRM; Montreal, Canada. 2011. p. 4515

66. Wisnieff C, Liu T, Spincemaille P, Wang S, Zhou D, Wang Y. Magnetic susceptibility anisotropy: cylindrical symmetry from macroscopically ordered anisotropic molecules and accuracy of MRI measurements using few orientations. NeuroImage. 2013; 70:363–376. [PubMed: 23296181]

67. Dieterich HJ, Barrett JM, Kriz W, Bulhoff JP. The ultrastructure of the thin loop limbs of the mouse kidney. Anat Embryol (Berl). 1975; 147(1):1–18. [PubMed: 1200392]

68. Merboldt KD, Hanicke W, Frahm J. Diffusion imaging using stimulated echoes. Magn Reson Med. 1991; 19(2):233–239. [PubMed: 1881309]

69. Tuch DS. Q-ball imaging. Magn Reson Med. 2004; 52(6):1358–1372. [PubMed: 15562495]

70. Wedeen, VJ., Reese, TG., Tuch, DS., Weigel, MR., Dou, J-G., Weiskoff, RM., Chessler, D. Mapping fiber orientation spectra in cerebral white matter with Fourier-transform diffusion MRI. Proceedings of the 8th Annual ISMRM; Denver, Colorado, USA. 2000. p. 82

71. Bonventre JV, Weinberg JM. Recent advances in the pathophysiology of ischemic acute renal failure. J Am Soc Nephrol. 2003; 14(8):2199–2210. [PubMed: 12874476]

72. Brezis M, Epstein FH. Cellular Mechanisms of Acute Ischemic-Injury in the Kidney. Annu Rev Med. 1993; 44:27–37. [PubMed: 8476249]

73. Devarajan P. Update on mechanisms of ischemic acute kidney injury. J Am Soc Nephrol. 2006; 17(6):1503–1520. [PubMed: 16707563]

74. Glaumann B, Glaumann H, Berezesky IK, Trump BF. Studies on cellular recovery from injury. II. Ultrastructural studies on the recovery of the pars convoluta of the proximal tubule of the rate kidney from temporary ischemia. Virchows Arch B Cell Pathol. 1977; 24(1):1–18. [PubMed: 405790]

75. Sharfuddin AA, Molitoris BA. Pathophysiology of ischemic acute kidney injury. Nat Rev Nephrol. 2011; 7(4):189–200. [PubMed: 21364518]

76. Glaumann B, Glaumann H, Trump BF. Studies of cellular recovery from injury. III. Ultrastructural studies on the recovery of the pars recta of the proximal tubule (P3 segment) of the rat kidney from temporary ischemia. Virchows Arch B Cell Pathol. 1977; 25(4):281–308. [PubMed: 413259]

77. Bovendeerd PHM, Arts T, Huyghe JM, van Campen DH, Reneman RS. Dependence of local left ventricular wall mechanics on myocardial fiber orientation: A model study. J Biomech. 1992; 25(10):1129–1140. [PubMed: 1400513]

78. Tezuka F. Muscle fiber orientation in normal and hypertrophied hearts. Tohoku J Exp Med. 1975; 117(3):289–297. [PubMed: 128157]

79. Wickline SA, Verdonk ED, Wong AK, Shepard RK, Miller JG. Structural remodeling of human myocardial tissue after infarction. Quantification with ultrasonic backscatter. Circulation. 1992; 85(1):259–268. [PubMed: 1728457]

80. Strijkers GJ, Bouts A, Blankesteijn WM, Peeters TH, Vilanova A, van Prooijen MC, Sanders HM, Heijman E, Nicolay K. Diffusion tensor imaging of left ventricular remodeling in response to myocardial infarction in the mouse. NMR Biomed. 2009; 22(2):182–190. [PubMed: 18780284]

81. Hsu, EW., Healy, LJ., Einstein, DR., Kuprat, AP. Imaging-Based Assessment and Modeling of the Structures of the Myocardium. In: Guccione, JM.Kassab, GS., Ratcliffe, MB., editors. Computational cardiovascular mechanics: modeling and applications in heart failure. New York, NY: Springer; 2010. p. 27

82. Hsu EW, Muzikant AL, Matulevicius SA, Penland RC, Henriquez CS. Magnetic resonance myocardial fiber-orientation mapping with direct histological correlation. Am J Physiol. 1998; 274(5 Pt 2):H1627–1634. [PubMed: 9612373]

83. Scollan DF, Holmes A, Winslow R, Forder J. Histological validation of myocardial microstructure obtained from diffusion tensor magnetic resonance imaging. Am J Physiol. 1998; 275(6 Pt 2):H2308–2318. [PubMed: 9843833]

84. Sosnovik DE, Mekkaoui C, Huang S, Chen HH, Dai G, Stoeck CT, Ngoy S, Guan J, Wang R, Kostis WJ, Jackowski MP, Wedeen VJ, Kozerke S, Liao R. Microstructural impact of ischemia and bone marrow-derived cell therapy revealed with diffusion tensor magnetic resonance imaging tractography of the heart in vivo. Circulation. 2014; 129(17):1731–1741. [PubMed: 24619466]

85. Sun Y, Zhang JQ, Zhang J, Lamparter S. Cardiac remodeling by fibrous tissue after infarction in rats. J Lab Clin Med. 2000; 135(4):316–323. [PubMed: 10779047]

86. Querejeta R, López B, González A, Sánchez E, Larman M, Martínez Ubago JL, Díez J. Increased Collagen Type I Synthesis in Patients With Heart Failure of Hypertensive Origin: Relation to Myocardial Fibrosis. Circulation. 2004; 110(10):1263–1268. [PubMed: 15313958]

87. Krasnosselskaia, LV. eMagRes. John Wiley & Sons, Ltd; 2007. Mechanisms for Short T2 and T2* in Collagen-Containing Tissue.

88. Krasnosselskaia LV, Fullerton GD, Dodd SJ, Cameron IL. Water in tendon: Orientational analysis of the free induction decay. Magn Reson Med. 2005; 54(2):280–288. [PubMed: 16032660]

89. Alford JW, Cole BJ. Cartilage restoration, part 1: basic science, historical perspective, patient evaluation, and treatment options. Am J Sports Med. 2005; 33(2):295–306. [PubMed: 15701618]

90. Xia Y, Moody JB, Alhadlaq H. Orientational dependence of T2 relaxation in articular cartilage: A microscopic MRI (microMRI) study. Magn Reson Med. 2002; 48(3):460–469. [PubMed: 12210910]

91. Bilgic B, Xie L, Dibb R, Langkammer C, Mutluay A, Ye H, Polimeni JR, Augustinack J, Liu C, Wald LL, Setsompop K. Rapid multi-orientation quantitative susceptibility mapping. NeuroImage. 2016; 125:1131–1141. [PubMed: 26277773]

92. Li X, van Zijl PCM. Mean magnetic susceptibility regularized susceptibility tensor imaging (MMSR-STI) for estimating orientations of white matter fibers in human brain. Magn Reson Med. 2014; 72(3):610–619. [PubMed: 24974830]

93. Li X, Vikram DS, Lim IA, Jones CK, Farrell JA, van Zijl PC. Mapping magnetic susceptibility anisotropies of white matter in vivo in the human brain at 7 T. NeuroImage. 2012; 62(1):314–330. [PubMed: 22561358]

94. Klette R, Toerring JT, Plato M, Moebius K, Boenigk B, Lubitz W. Determination of the g tensor of the primary donor cation radical in single crystals of Rhodobacter sphaeroides R-26 reaction centers by 3-mm high-field EPR. J Phys Chem. 1993; 97(9):2015–2020.

95. Wu B, Li W, Avram AV, Gho SM, Liu C. Fast and tissue-optimized mapping of magnetic susceptibility and T2* with multi-echo and multi-shot spirals. NeuroImage. 2012; 59(1):297–305. [PubMed: 21784162]

96. Hebert, SC. Compr Physiol. John Wiley & Sons, Inc; 2010. Nephron Heterogeneity.

97. Kaissling B, Kriz W. Morphology of the Loop of Henle, Distal Tubule, and Collecting Duct. Compr Physiol. 2011:109–167.

98. Maunsbach, AB., Christensen, EI. Compr Physiol. John Wiley & Sons, Inc; 2010. Functional Ultrastructure of the Proximal Tubule.

99. Schwartz MM, Venkatachalam MA. Structural differences in thin limbs of Henle: physiological implications. Kidney Int. 1974; 6(4):193–208. [PubMed: 4427417]

100. Nordhoy W, Anthonsen HW, Bruvold M, Brurok H, Skarra S, Krane J, Jynge P. Intracellular manganese ions provide strong T1 relaxation in rat myocardium. Magn Reson Med. 2004; 52(3):506–514. [PubMed: 15334568]

101. Dibb R, Li W, Cofer G, Liu C. Microstructural origins of gadolinium-enhanced susceptibility contrast and anisotropy. Magn Reson Med. 2014; 72(6):1702–1711. [PubMed: 24443202]

102. Adzamli IK, Jolesz FA, Bleier AR, Mulkern RV, Sandor T. The effect of gadolinium DTPA on tissue water compartments in slow- and fast-twitch rabbit muscles. Magn Reson Med. 1989; 11(2):172–181. [PubMed: 2779410]

103. Magnusson SP, Hansen P, Kjaer M. Tendon properties in relation to muscular activity and physical training. Scand J Med Sci Sports. 2003; 13(4):211–223. [PubMed: 12859603]

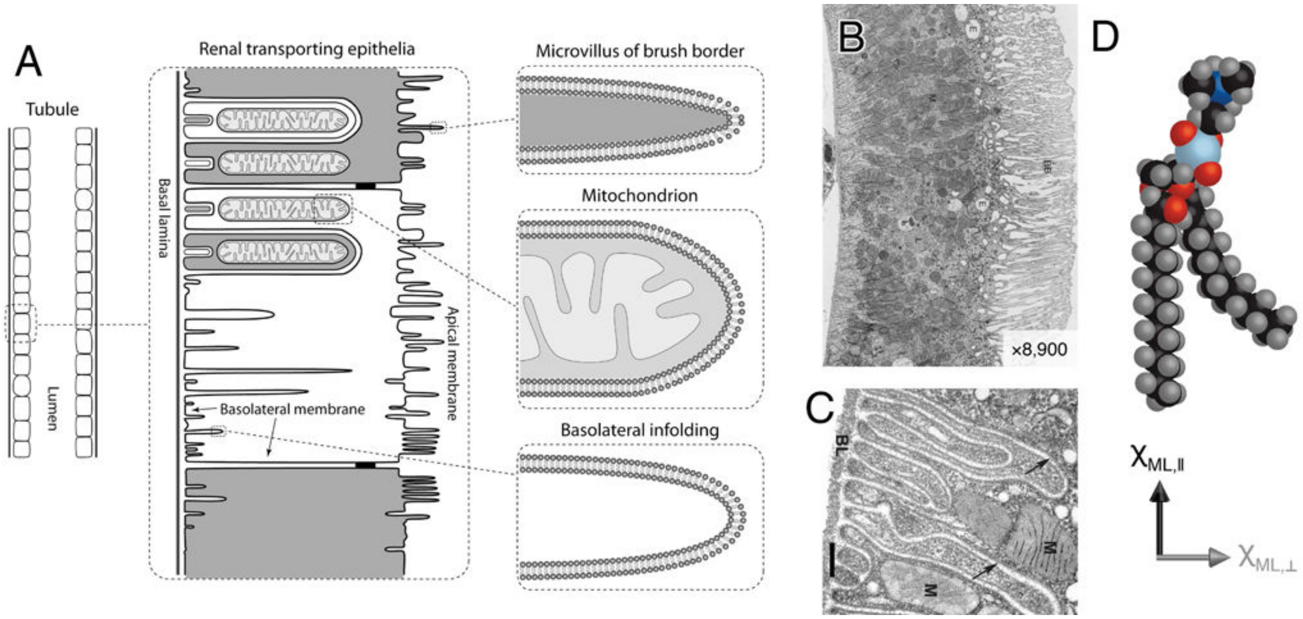

Fig. 1.

Molecular and microstructural basis of susceptibility anisotropy in the renal tubule. (A) Essential structural features of the renal transporting epithelia. The diagram insets accentuate the lipid bilayer in the microvillus of the brush border, the mitochondrion, and the basolateral infolding. (B) Electron micrograph of rat epithelium showing the brush border. Mitochondria are oriented perpendicular to the basement membrane. (C) Transmission electron micrograph of interdigitated lateral folds and neighboring mitochondria (M) perpendicular to the basal lamina (BL). Scale bar = 100 nm. (D) Individual phospholipids are more diamagnetic in the direction parallel to the chain structure than in perpendicular direction. Figure is adapted with permissions from (21,37,98).

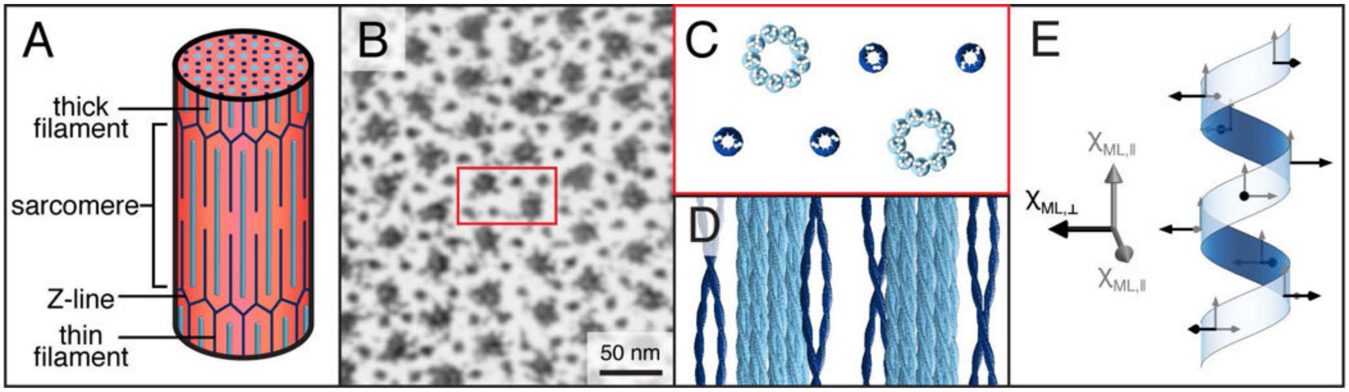

Fig. 2.

Molecular and microstructural basis of susceptibility anisotropy in the myofibril. (A) Diagram of a cardiac myofibril segment showing the serially repeating sarcomere unit, which lies between two Z-lines. (B) An electron microscopy image of a cross-section of the sarcomere highlights the myofilament lattice in myocardial tissue (image courtesy of Margaret Goldstein, PhD, Baylor College of Medicine and Robert Perz-Edwards, PhD, Duke University). (C) A rendering of myosin and tropomyosin in the myofilament lattice section highlighted by the red box in (B) that repeats throughout the sarcomere. (D) Thick (light blue) and thin (dark blue) filaments are represented by the secondary and tertiary α-helical structures. (E) The α-helix peptide groups lie in a plane that runs parallel to the helix axis. For each individual peptide group, the molecular level out-of-plane susceptibility (black arrow) is more diamagnetic than the in-plane susceptibility (gray arrows). Figure is adapted from (17).

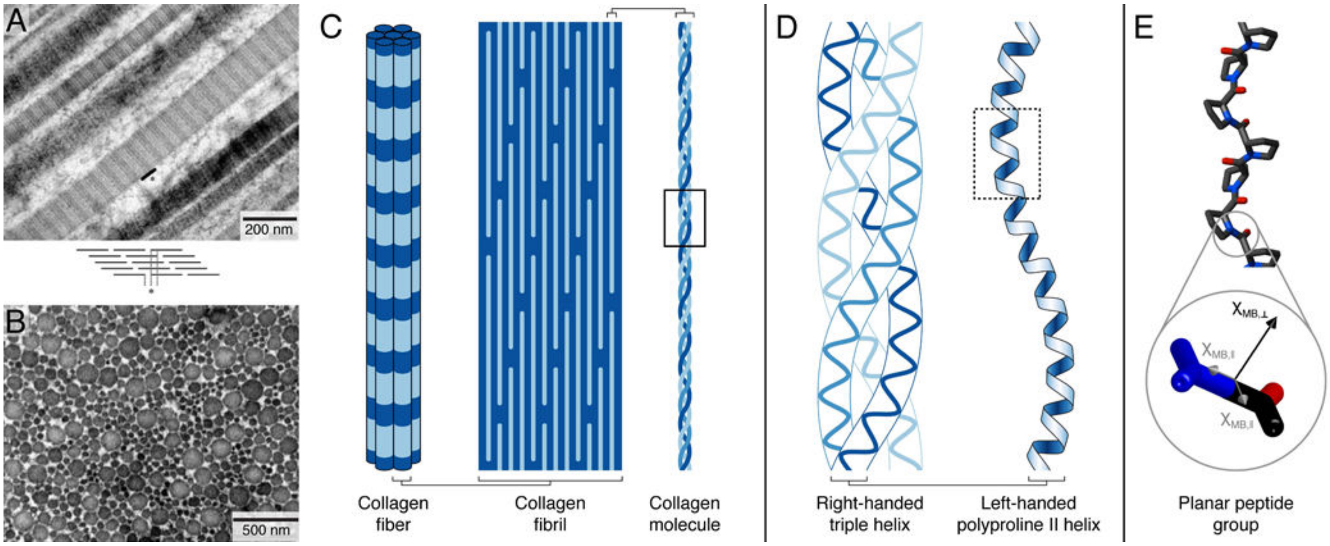

Fig. 3.

Molecular and microstructural basis of susceptibility anisotropy in collagen. Electron microscopy of (A) longitudinal and (B) transverse sections of human Achilles tendon fibrils (images used with permission from (103)). The black marker (*) corresponds to the length of one repeating light and dark band, which together represent the axial 67 nm *D*-periodization of collagen fibrils. (C) A collagen fiber is composed of many fibrils. The light and dark bands within an individual fibril correspond to overlap and gap regions of collagen molecules. (D) A zoomed-in view of the solid rectangle from (C) shows the detail of the right-handed triple helix structure. The triple helix structure is composed of left-handed polyproline II-type helices. (E) A zoomed-in view of the dotted rectangle in (D) highlights the planar peptide groups in the polyproline helix, which have an out-of-plane susceptibility (black arrow) that is more diamagnetic than the in-plane susceptibility (gray arrows).

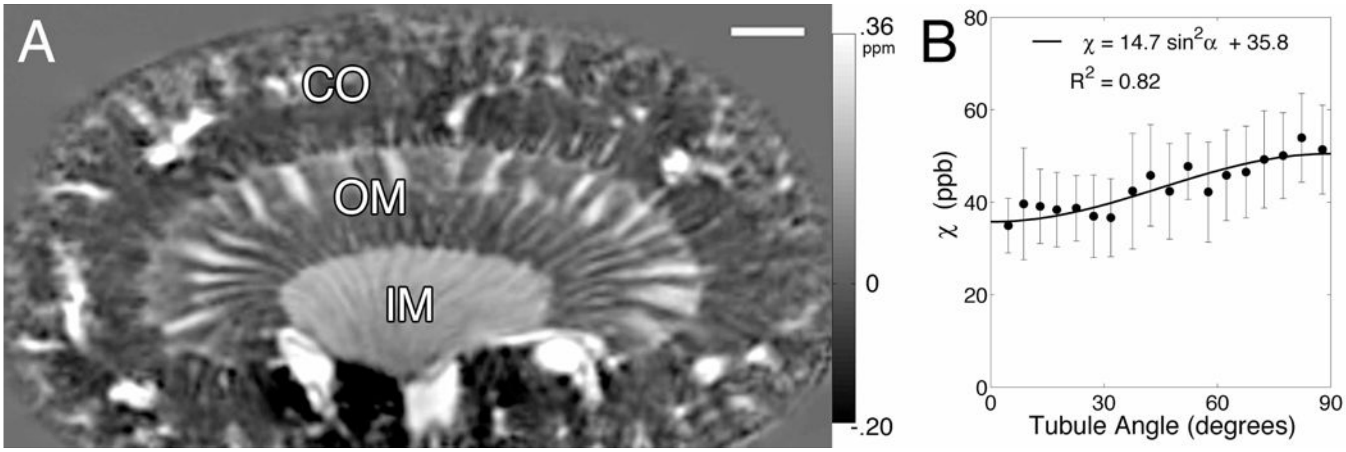

Fig. 4.

Measuring susceptibility anisotropy of the renal tubule using multi-orientation QSM and DTI. (A) Representative QSM of the kidney at one field orientation shows the susceptibility contrast between the inner medulla (IM), outer medulla (OM), and cortex (CO). MR phase image data were acquired from an excised mouse kidney with contrast agent at 12 orientations using a 3-D spoiled GRE sequence with 6 echoes ($TE_1/\Delta TE/TE_6$ = 3.4/2.9/17.9 ms, TR = 50 ms, α = 50°, array size = 256 × 256 × 256, isotropic voxel size = 55 μm, scan time per orientation = 0.9 hours). Tubule orientation was calculated from the principal eigenvector of diffusion tensor data. (B) Susceptibility values as a function of tubule angle between the major eigenvector of the diffusion tensor and B_0. Susceptibility values (χ) are determined in the IM region and expressed in units of ppb (both y-axis and equation). Error bars represent one standard deviation within each bin. Scale bar = 1 mm. Figure used with permission from (21).

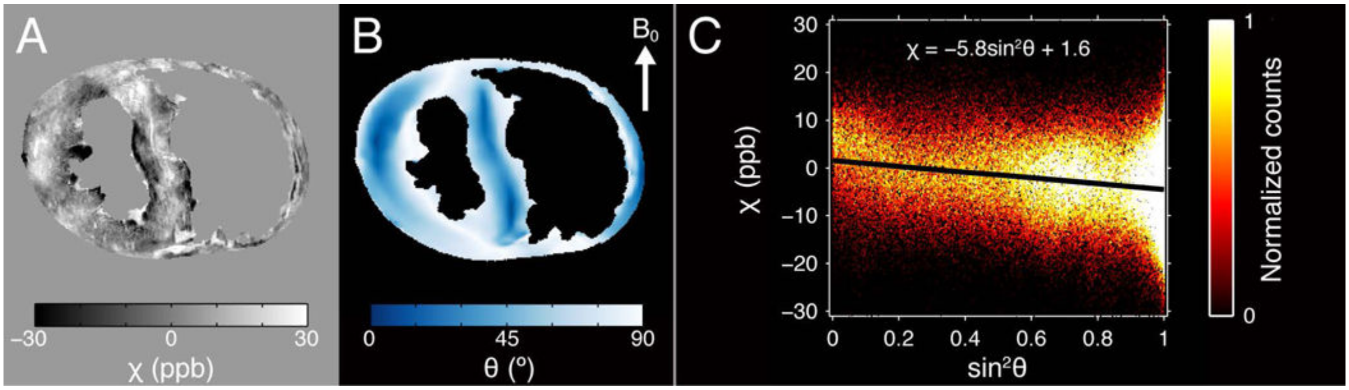

Fig. 5.

Detecting susceptibility anisotropy in myofibers using single-orientation QSM and DTI. (A) QSM calculated from MR phase image data acquired using a 3-D spoiled GRE sequence with 16 echoes ($TE_1/\Delta TE/TE_{16}$ = 1.7/3.0/46.7 ms, TR = 200 ms, α = 35°, array size = 256 × 256 × 256, isotropic voxel size = 45 μm, scan time = 3.6 hours). (B) Myofiber orientation with respect to B_0 was calculated from the principal eigenvector of diffusion tensor data (one image with b = 0 s/mm^2, 12 diffusion-encoded images with diffusion time = 5.5 ms, pulse separation = 17.0 ms, b = 1850 s/mm^2, TE = 23.6 ms, TR = 2000 ms, array size = 64 × 64 × 64, isotropic voxel size = 180 μm total scan time = 29.6 hours). (C) Two-dimensional histogram of the voxelwise apparent magnetic susceptibility as a function of the squared sine of the myofiber angle. The black line represents the fitted correlation described by the equation. Figure adapted from (17).

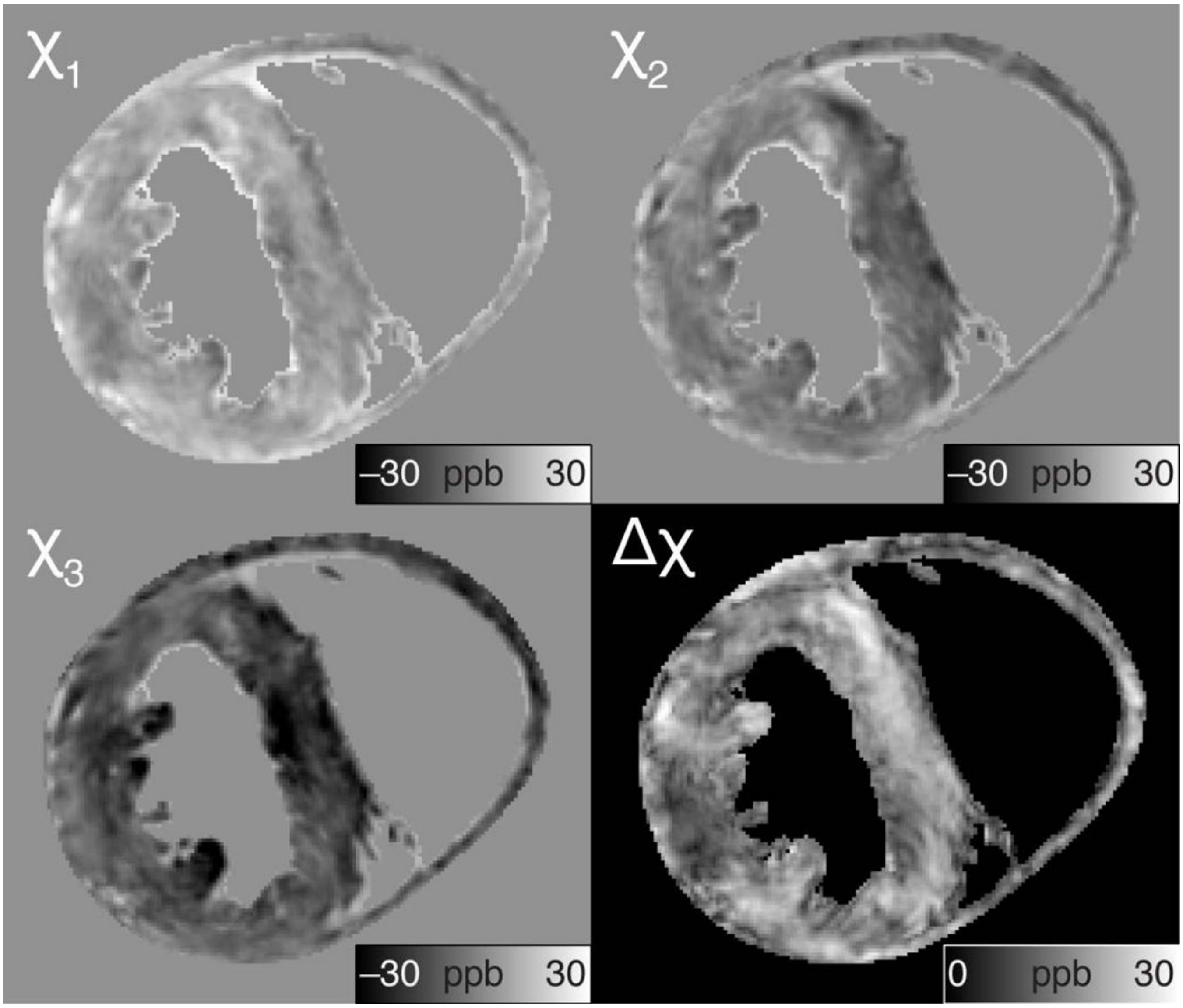

Fig. 6.

STI reconstruction of an excised mouse heart. The specimen was prepared by perfusion fixation via jugular vein, after which the chambers of the heart were filled with agarose gel according to the protocol in (17). MR magnitude and phase image data were acquired at 12 specimen orientations using a 3-D spoiled GRE sequence with 16 echoes ($TE_1/\Delta TE/TE_{16}$ = 2.2/4.2/65.2 ms, TR = 150 ms, α = 35°, array size = 400 × 300 × 300, isotropic voxel size = 45 μm, scan time per orientation = 3.75 hours). Following eigen decomposition of the susceptibility tensor, the primary (χ_1), secondary (χ_2), and tertiary (χ_3) eigenvalues were used to calculate bulk susceptibility anisotropy ($\Delta\chi$).

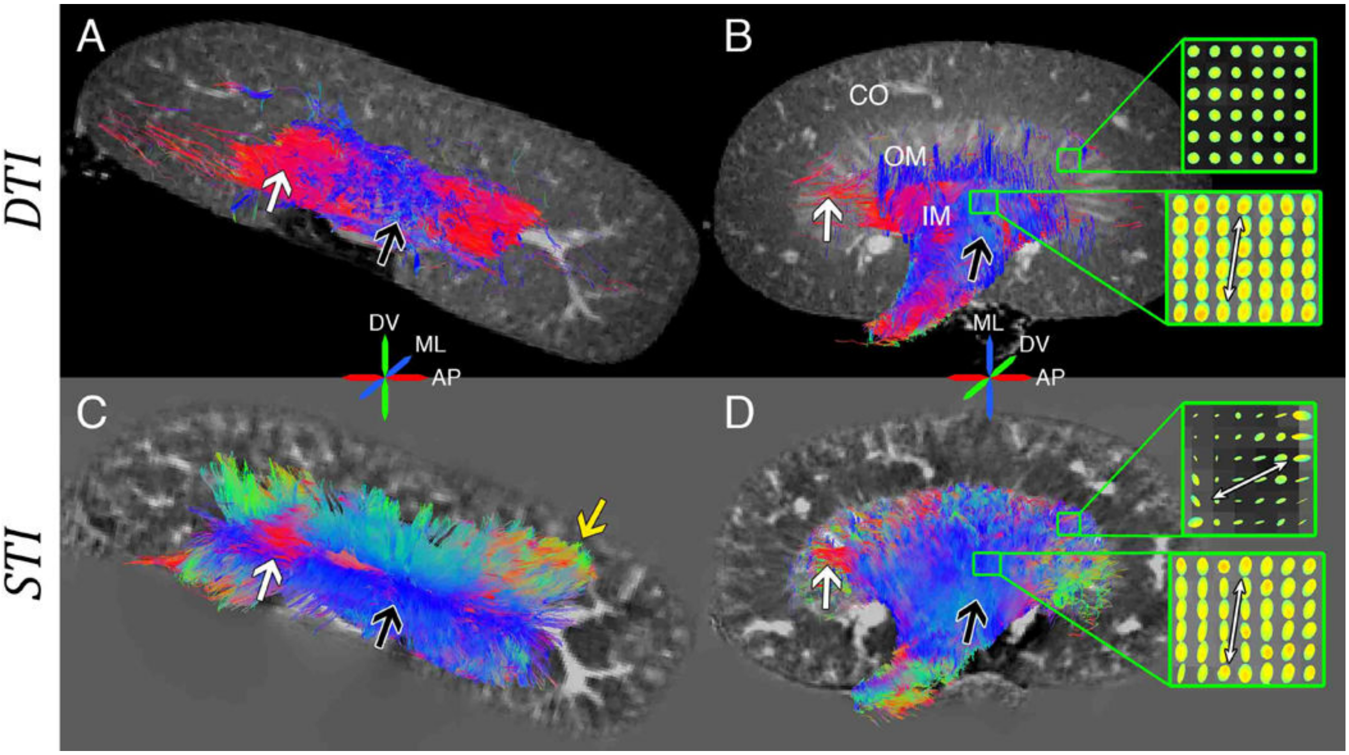

Fig. 7.

Tractography from DTI and STI in medullary regions of the kidney. (A–B) DTI tracts overlay the b_0 image and (C–D) STI tracts overlay the susceptibility trace image. (A,C) Sagittal view from outer medulla (OM) towards papilla tip. (B,D) Coronal view shows that both DTI and STI detect tubules in the inner medulla (IM) but not the cortex (CO). Black arrows point to tracts in mediolateral (ML) direction and white arrows point to tracts in anteroposterior (AP) direction. Yellow arrow indicates additional STI tracts in dorsoventral (DV) direction. Insets show tensor glyphs. White arrows in the insets point in the overall direction of glyphs. Figure is used with permission (21).

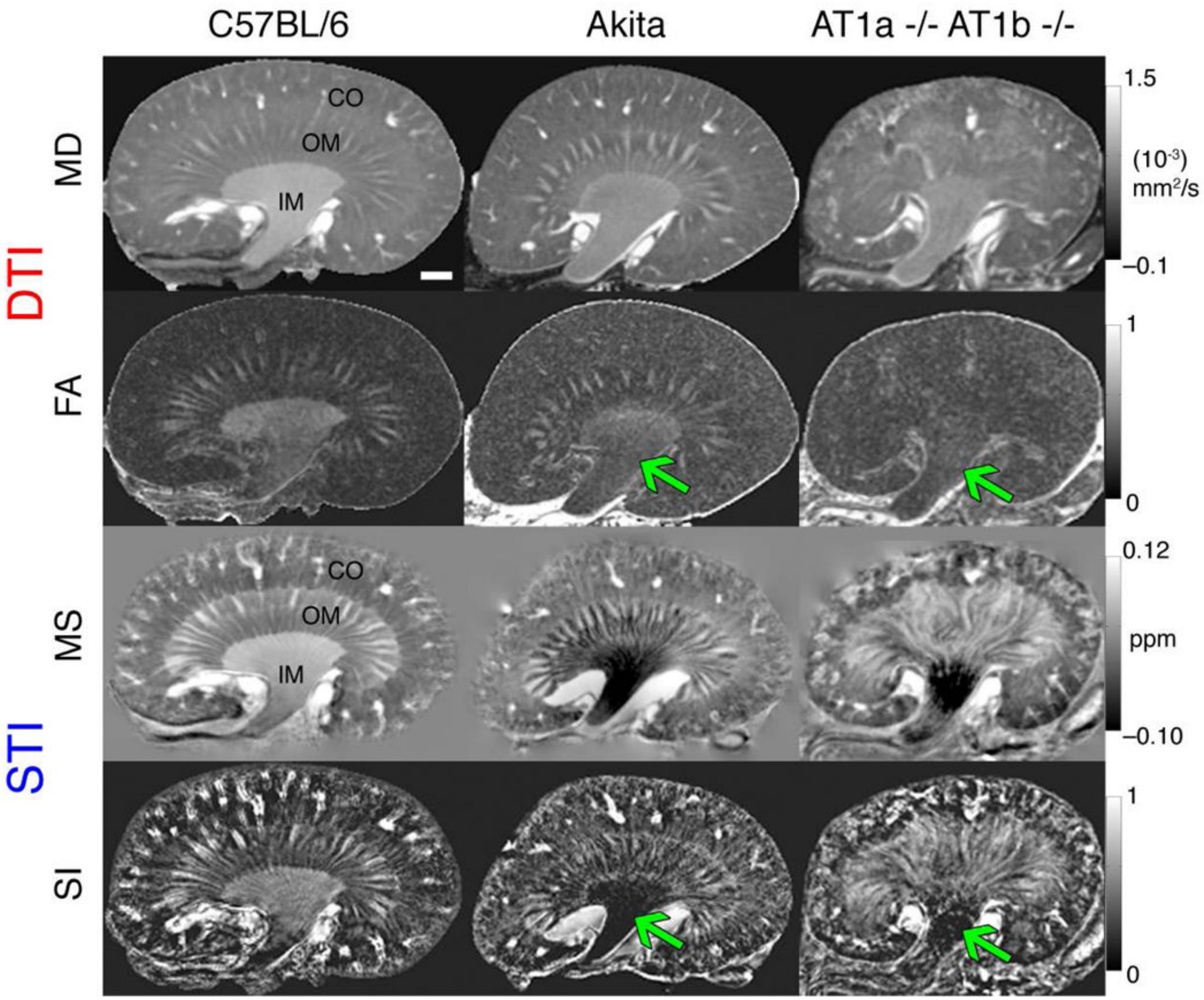

Fig. 8.

Comparison of DTI and STI in healthy and diseased mouse kidneys. Columns left to right: C57BL/6 (wild type), Akita (diabetic nephropathy), and AT1a −/− AT1b −/− (angiotensin receptor knockout). Rows top to bottom: mean diffusivity (MD) from DTI, fractional anisotropy (FA) from DTI, mean susceptibility (MS) from STI, and susceptibility index (SI) from STI (γ = 0). Green arrows point to anisotropic diffusion and susceptibility changes in the inner medulla (IM) of diseased kidneys. Susceptibility changes are subtler in the outer medulla (OM) and cortex (CO). Scale bar = 1 mm. Figure is adapted with permission (20).

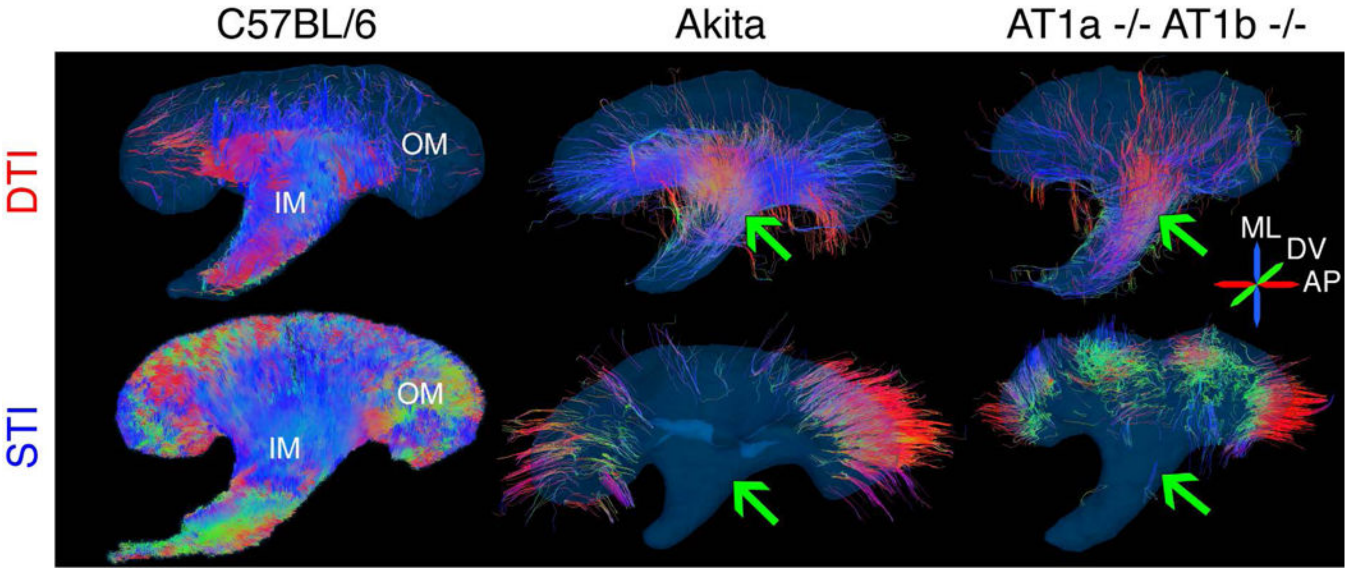

Fig. 9.

DTI- and STI-based tractography in healthy and diseased mouse kidneys. Columns left-to-right: C57BL/6 (wild type), Akita (diabetic nephropathy), and AT1a −/− AT1b −/− (angiotensin receptor knockout). Rows top-to-bottom: DTI and STI. Green arrows point to the inner medulla (IM) of diseased kidneys where DTI and STI tracts are markedly reduced. The number of STI tracts in the outer medulla (OM) is also reduced in the disease models. AP = Anteroposterior, DV = dorsoventral, ML = mediolateral. Figure is adapted with permission (20).

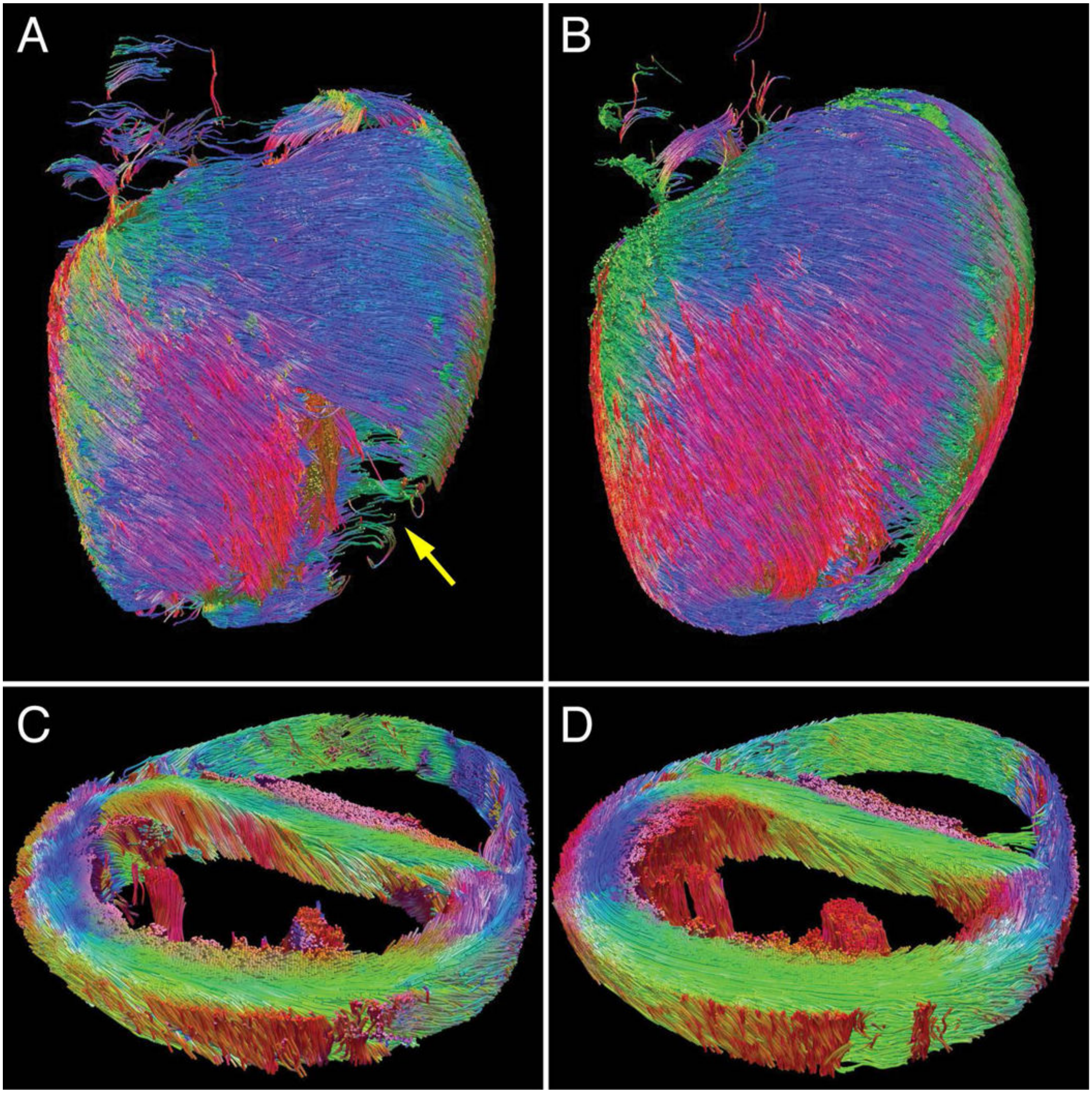

Fig. 10.

Myofiber tractography derived from MRI of a mouse heart specimen (18). The continuity and consistency of tracts (> 1 mm in length) from (A) susceptibility-based tensor data compare well to (B) diffusion tensor data, except in the thinnest regions of the right ventricle wall (yellow arrow). A 1-mm thick segment reveals that tract orientations in (C) susceptibility-based tensor data closely resemble those from (D) diffusion tensor data.

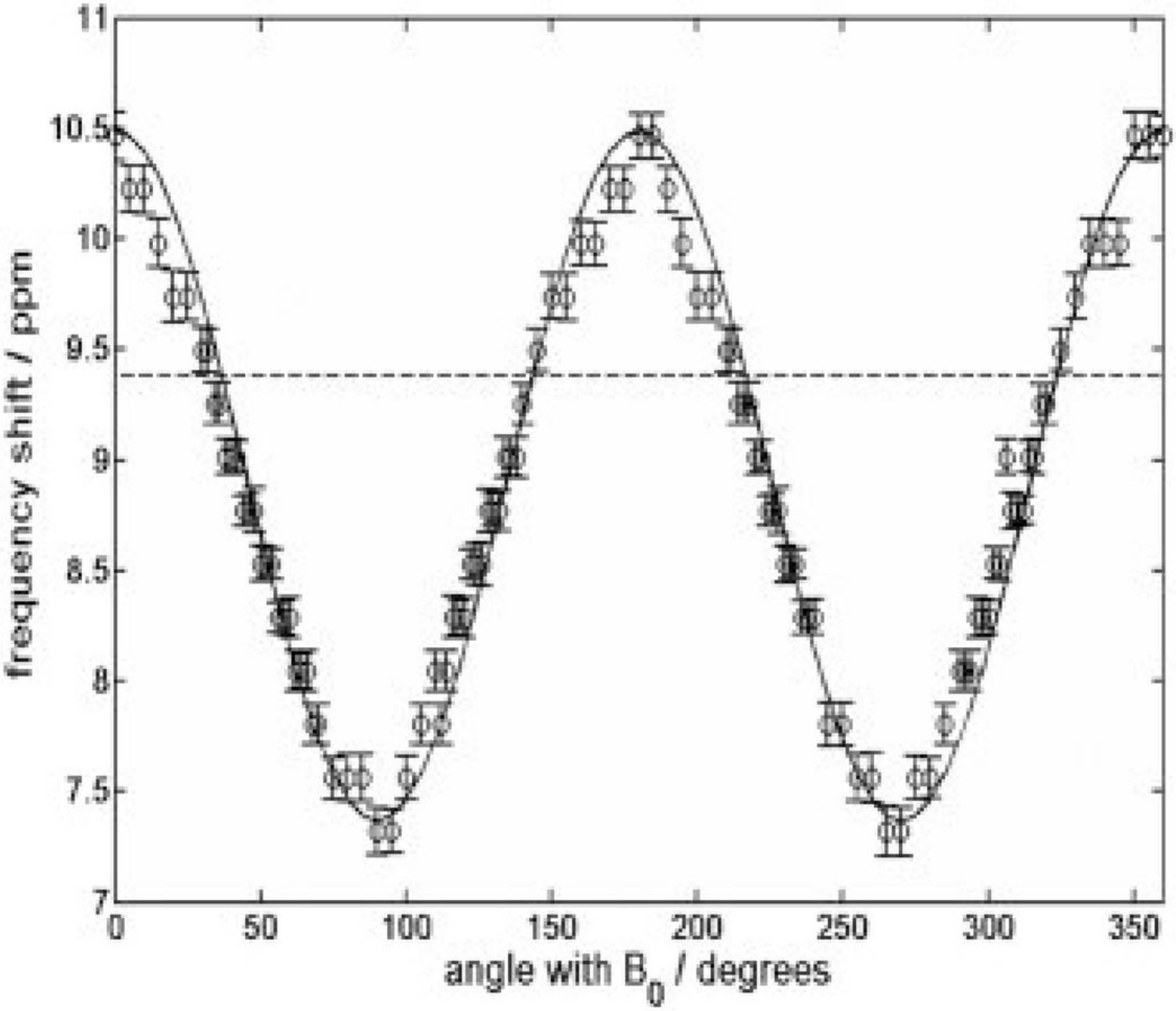

Fig. 11.

Central frequency shift as a function of bovine tendon orientation, Θ. The central frequency was determined as the frequency of the maximum amplitude of the Fourier-transformed FID. Circles: experimentally obtained values. The solid line is a fit to the function: $f(\Theta) = a_1 y + a_2$, where $y = (1/2)(3 \cos^2(\pi/2) + \Theta) - 1)$, $a_1 = -2.08$, and $a_2 = 9.45$. Error bars are 10% of the central line width. The dashed line is the position of a water peak in the external reference sample. Figure obtained with permission from (88).

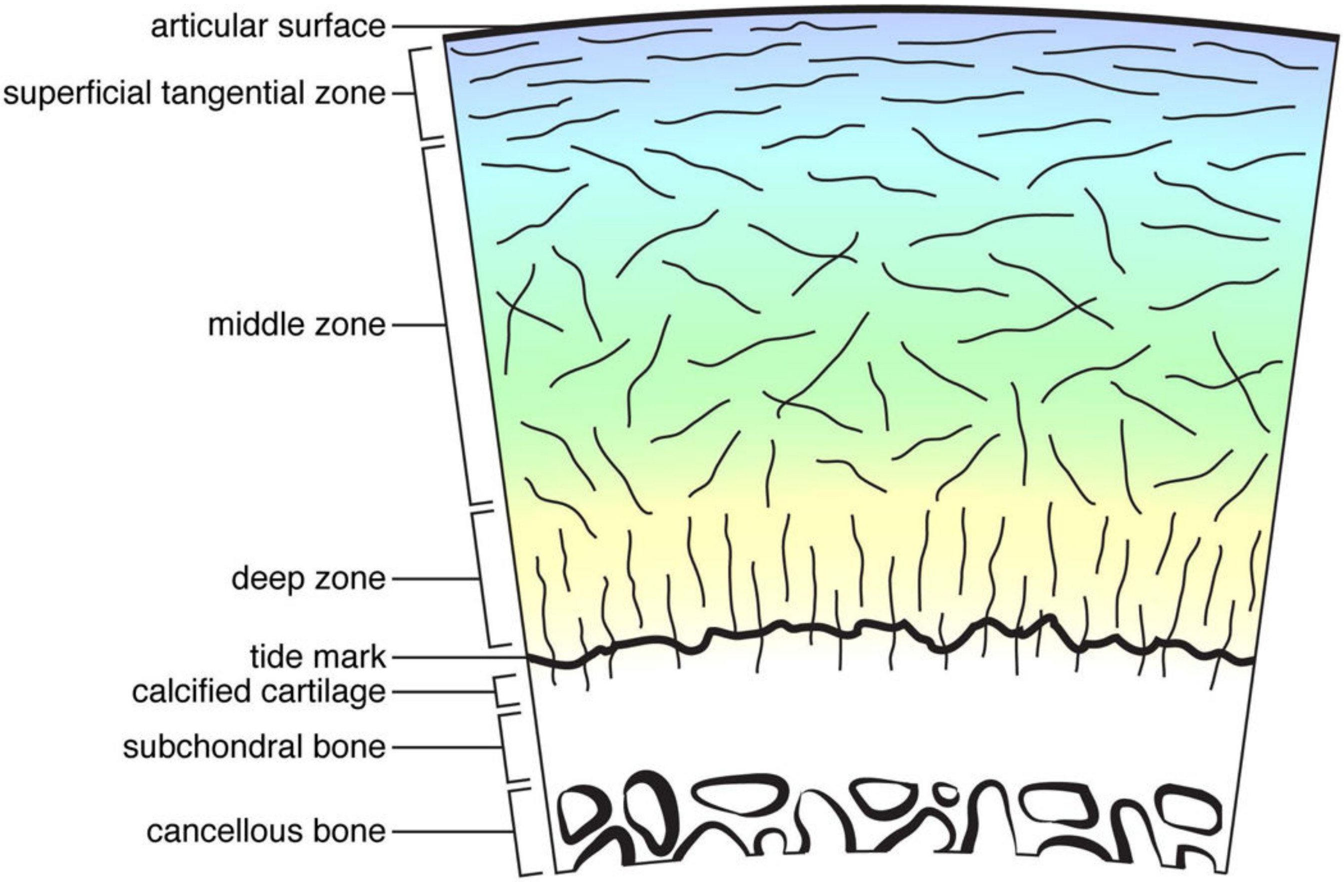

Fig. 12.

(A) Diagram of articular cartilage layers highlighting the collagen fiber orientation of the superficial tangential, middle, and deep cartilage zones. The tangentially oriented collagen fibers in the superficial layers resist shear, whereas the more vertically oriented fibers in the deeper layers resist compression. The calcified layers (tide mark and calcified cartilage) adhere the cartilage to bone.

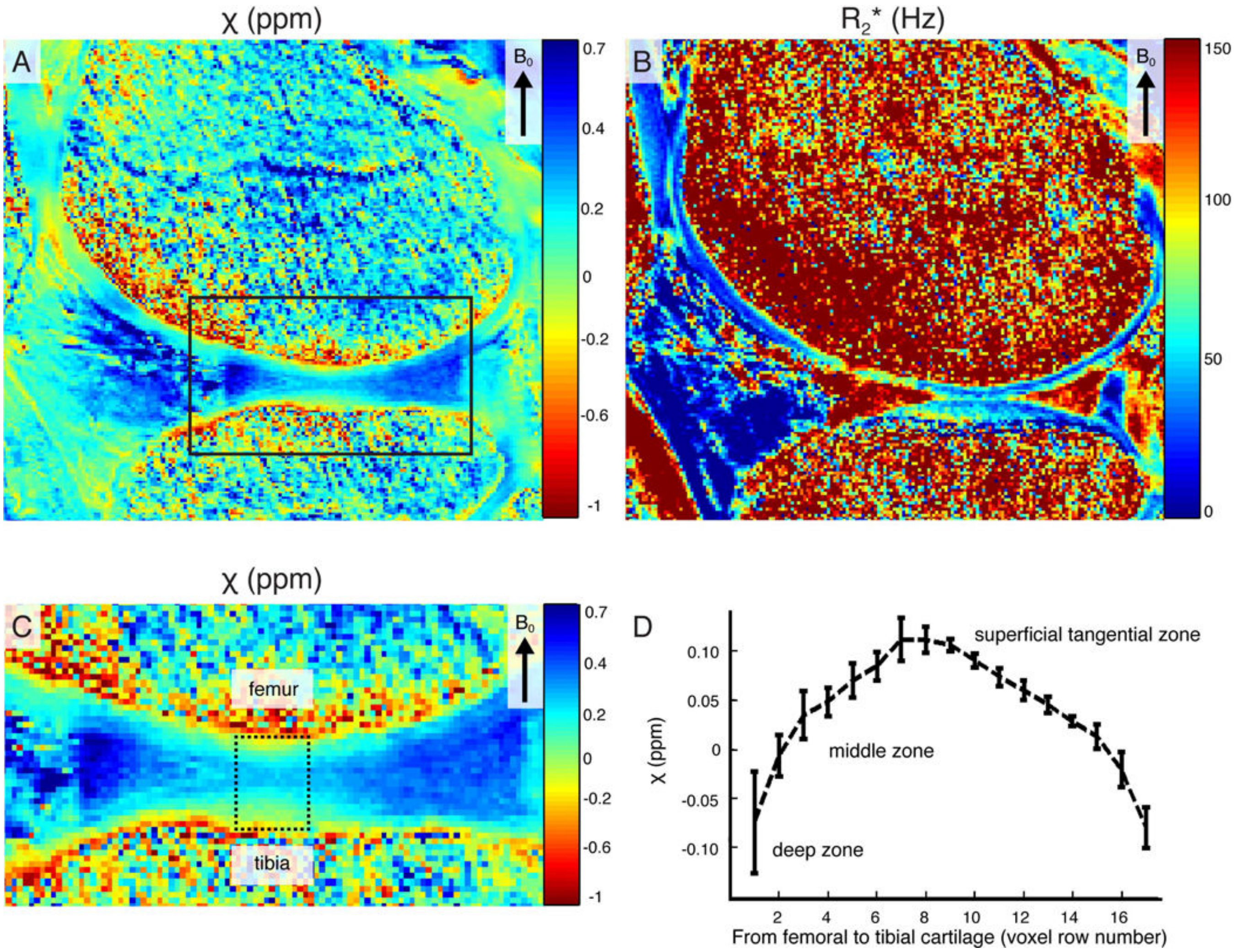

Fig. 13.

QSM reveals the layers of articular cartilage in the knee joint. Color maps of (A) QSM and (B) R_2* from the knee joint in a healthy, 30-year-old male. Multi-echo GRE image data were acquired using the following scan parameters: TE = [2.2, 2.5, 2.8, 4.4, 4.7, 5.0] ms, TR = 35 ms, α = 15°, bandwidth = ±651 kHz, array size = 380 × 384 × 88, voxel size = 0.4 × 0.4 × 1.6 mm^3, GRAPPA factor = three, total scan time = 16 minutes. (C) A detailed view of the solid black rectangle in (A) exhibits the susceptibility variation in articular cartilage. (D) Susceptibility values are plotted against the vertical position from femoral to tibial cartilages within the dotted black rectangle in (C). The size of the box is 17 × 10 (row × column). Each χ value in the plot represents the mean of all 10 voxels in one row. The rows are numbered from femur bone surface to tibia bone surface. Figure is adapted from (22).

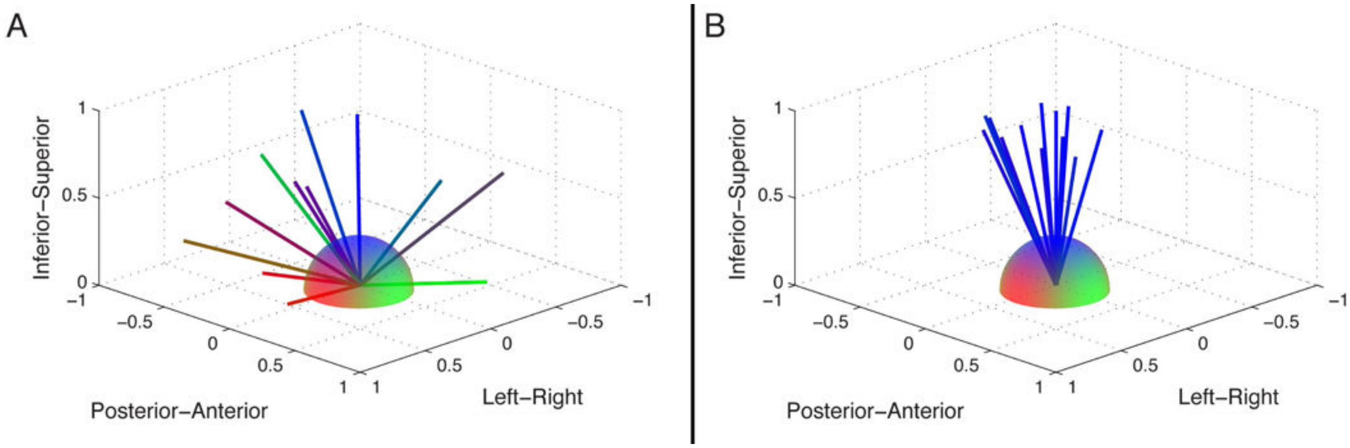

Fig. 14.

STI orientation sampling. The unit vectors of 12 object orientations are shown for (A) an *ex vivo* study of the mouse kidney and (B) an *in vivo* study of the human brain. B_0 is aligned with the inferior-superior direction.

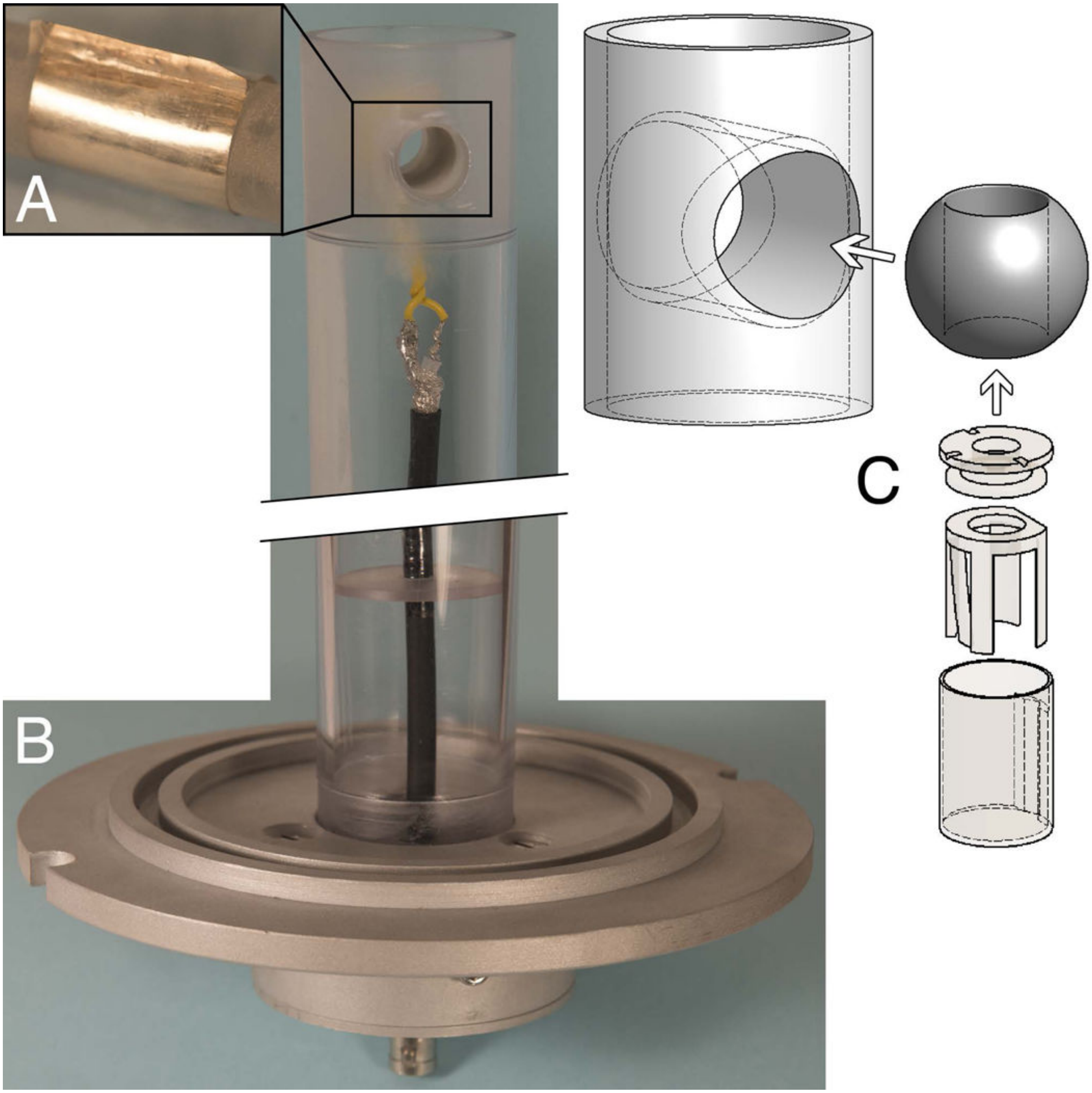

Fig. 15.

Hardware designed for preclinical STI at 9.4 T of tissues and organs as large as the mouse kidney and heart. (A) Inset showing a silver solenoid coil inside the tube. (B) Center shielded cable connects to the pick-up loop adjacent to the RF solenoid resonator. (C) Drawing of the cartridge that contains the immersed specimen. The cartridge is placed inside the sphere, which may be manually repositioned to any orientation inside the coil. Parts are not drawn to scale. Figure is adapted with permission (21).

Table 1

Comparison of DTI and STI on straight nephron segments of the mouse kidney. Inner diameters are approximated from previous literature (37,98).

Segment	**Inner diameter (μm)**	**DTI**	**STI**
Ascending thin loop	~ 10	*	*
Medullary thick ascending limb	> 47		*
Collecting ducts	> 50		*

[*] detectable length scale